Colloidal quantum dot lasers

Young-Shin Park[1,2], *Jeongkyun Roh*[1,3], *Benjamin T. Diroll*[4], *Richard D. Schaller*[4,5] *and Victor I. Klimov*[1] ✉

Abstract | Semiconductor nanocrystals represent a promising class of solution-processable optical-gain media that can be manipulated via inexpensive, easily scalable colloidal techniques. Due to their extremely small sizes (typically <10 nm), their properties can be directly controlled via effects of quantum confinement; therefore, they are often termed colloidal quantum dots (CQDs). In addition to size-tunable emission wavelengths, CQDs offer other benefits for lasing applications, including low optical-gain thresholds and high temperature stability of lasing characteristics. Recent progress in understanding and practical control of processes impeding light amplification in CQDs has resulted in several breakthroughs, including the demonstration of optically pumped continuous-wave lasing, the realization of optical gain with direct current electrical injection and the development of dual-function electroluminescent devices that also operate as optically pumped lasers. The purpose of this Review is to assess the status of the field of CQD lasing and discuss the existing challenges and opportunities. A particular focus is on approaches for suppressing nonradiative Auger recombination, novel optical-gain concepts enabled by strong exciton–exciton interactions and controlled CQD charging, effects of nanocrystal form factors on light amplification and practical architectures for realizing electrically pumped CQD lasers. This overview suggests that the accumulated knowledge, along with the approaches developed for manipulating the optical-gain properties of colloidal nanostructures, perfectly position the CQD field for successfully addressing a long-standing challenge: the realization of CQD-based laser diodes.

Existing semiconductor lasers, or laser diodes, are based on one or multiple ultra-thin semiconductor layers, or quantum wells, incorporated into a light-emitting-diode (LED)-like structure for charge injection. Despite the tremendous success of lasers based on epitaxially grown semiconductors, there are certain technologies that could benefit from the availability of lasers based on solution-processable materials. These include integrated photonic circuits[1–4], optical interconnects[5–7], lab-on-a-chip platforms[8,9], wearable[10–12] and advanced medical[13–16] devices, clandestine markers[10] and many others. A promising class of solution-processable gain media is semiconductor nanocrystals prepared via inexpensive, easily scalable colloidal techniques[17–21]. Owing to their extremely small sizes (a few nanometres across), these structures allow one to access the regime of quantum confinement, in which the properties of a material become directly dependent on its size. Typically, this regime is realized when at least one dimension of a nanostructure is comparable to or smaller than an exciton Bohr radius of its parental bulk solid. When this condition is satisfied for all three dimensions, the resulting material represents a 0D nanostructure, a quantum dot (QD).

Early studies of nanocrystals utilized samples prepared by high-temperature precipitation in molten glasses[22–25]. Eventually, the focus of nanocrystal research shifted to semiconductor particles fabricated via colloidal chemical methods that allow for atomic-level control of nanostructure dimensions, shape and internal structure[17,26–29]. Colloidal nanocrystals can exhibit a variety of morphologies, from nanospheres[30–32] and nanocubes[33,34] to elongated nanorods[27,35,36], flat nanoplatelets (NPLs)[37–39] and branched tetrapods[40–42]. If all their dimensions are quantum confined, such structures can be treated as a 0D material; therefore, here, they are referred to as colloidal QDs (CQDs), independent of their shape. By contrast, long nanorods exhibit properties typical of 1D structures, whereas large-area, thin NPLs behave as 2D quantum wells. In such cases, we explicitly indicate the morphology of the structure under discussion.

Recently, there has been considerable progress in the manipulation of the optical-gain properties of CQDs using, for example, photochemical charging for suppressing ground-state absorption[43,44] and compositional grading for impeding nonradiative Auger decay[45–47]. These advances have allowed for several

[1]*Chemistry Division, Los Alamos National Laboratory, Los Alamos, NM, USA.*

[2]*Centre for High Technology Materials, University of New Mexico, Albuquerque, NM, USA.*

[3]*Department of Electrical Engineering, Pusan National University, Busan, Republic of Korea.*

[4]*Centre for Nanoscale Materials, Argonne National Laboratory, Lemont, IL, USA.*

[5]*Department of Chemistry, Northwestern University, Evanston, IL, USA.*

✉*e-mail: klimov@lanl.gov*

https://doi.org/10.1038/s41578-020-00274-9

breakthroughs in CQD lasing, including the development of optically pumped continuous-wave (cw) lasers[48], the realization of optical gain with direct current (d.c.) electrical injection[49], the demonstration of low-threshold, sub-single-exciton lasing[43] and the practical implementation of dual-function devices operating as both a standard LED and an optically pumped laser[50]. These exciting developments suggest that the long-standing objective of CQD research, which is the realization of electrically pumped lasing devices, is within close reach.

The optical gain and lasing properties of CQDs have been previously discussed as part of dedicated reviews on this subject[51,52], as well as broader overviews of colloidal nanostructures[18,53,54]. The purpose of this Review is to update the reader on the most recent advances in the CQD lasing field, with a focus on distinctive features of the optical-gain regime specific to CQDs, the methods for controlling processes impeding light amplification, novel lasing concepts implemented with colloidal nanomaterials and device aspects of optically and electrically pumped CQD lasers.

Quantum dots as lasing materials

Implications of 0D confinement for lasing. A general feature of QDs is a size-tunable band gap, E_g (FIG. 1a). For spherical particles with radius R, the quantum-confinement-induced shift of the band gap, $\Delta E_{conf} = E_g - E_{g,bulk}$, is approximately proportional to $1/R^2$ (REFS[55,56]); here, $E_{g,bulk}$ is the band gap of the bulk material. The variation in E_g achievable through the quantum size effect is especially large for colloidal nanocrystals, whose mean radius can be in the range 1–10 nm. The size-dependent band gap allows one to readily tune the emission wavelength by simply changing the size of the particle, which has been exploited in CQD-based commercial displays and televisions.

Facile colour tunability of CQD emission is also attractive for lasing applications, as it could help fill the gaps in the colour space not accessible with existing semiconductor laser diodes. For example, using II–VI CQDs, it is possible to realize the regime of light amplification across the entire visible wavelength range. This capability is illustrated by the example in FIG. 1b, which shows multicolour amplified spontaneous emission (ASE) from CdSe-based CQDs, tunable from 690 nm (red) to 520 nm (green)[57].

In addition to the size-dependent band gap, a distinctive property of 0D materials is their atomic-like, discrete energy levels. As was originally pointed out in REF.[58], this feature is beneficial to lasing applications, because a wide separation between electronic states inhibits thermal depopulation of the band-edge electron and hole levels (FIG. 1a) and, thereby, reduces the lasing threshold compared with bulk materials and nanostructures of higher dimensionality. This property of QDs is illustrated by calculations of threshold current densities (j_{las}, FIG. 1c) conducted for four different materials morphologies (box, wire, film and bulk) that correspond, respectively, to 0D, 1D, 2D and 3D structures[59].

The discrete character of QD electronic states also improves the temperature stability of lasing devices[58]. This property is illustrated by the dependence of the optical-gain threshold on temperature for spherical QDs with radii between 1 and 20 nm (FIG. 1d). The optical-gain threshold is defined in terms of an average per-dot number of electron–hole (e–h) pairs (excitons), $\langle N \rangle$, calculated from the standard condition, $\phi_e + \phi_h = 0$ (REF.[60]), where ϕ_e and ϕ_h are, respectively, electron and hole quasi-Fermi potentials (referenced versus the respective band-edge states) computed using a single-band effective mass approximation[49]. At low temperature ($T < 5$ K), for all QD sizes, the gain threshold, $\langle N_{gain} \rangle$, is near the ideal value of 1 exciton per dot[61] ($\langle N_{gain} \rangle \approx 1$). However, the gain threshold sharply grows as the temperature passes the critical value T_0, defined as the temperature at which $\langle N_{gain} \rangle = 2$. Importantly, T_0 rapidly increases with decreasing QD size (inset of FIG. 1d), indicating that smaller QDs provide greater temperature stability for lasing-related properties.

Early research into quantum dot lasing. Prospective applications of 0D structures in lasing have motivated substantial research since the early days of QD science. The first indications of optical gain and ASE in QDs were revealed by picosecond transient absorption studies of glass-embedded CdSe nanocrystals[24]. These observations were followed by the demonstration of a true lasing action using CdSe QD/glass samples incorporated into a Fabry–Pérot cavity, reported in 1991 (REF.[25]) (FIG. 1e). Three years later, lasing was realized with self-assembled III–V epitaxial QDs using optical and then electrical pumping[62,63]. Follow-up developments resulted in impressive advances in the performance of epitaxial QD lasers and enabled the demonstration of record low lasing thresholds[64] and unprecedented temperature stability up to $T = 493$ K (220 °C) (REF.[65]).

The early studies of QD lasing using glass-based and epitaxially grown samples employed fairly large structures (~10 nm or bigger) that were not strongly affected by nonradiative multiexciton Auger recombination. The role of this process is greatly enhanced in small colloidal particles[66], which delayed the demonstration of lasing with CQDs. It took several years to uncover the connection between optical gain and multiexcitonic species and understand the resulting complications arising from nonradiative Auger decay[61,66]. Only after that, in 2000, colour-tunable ASE was realized with size-controlled CdSe CQDs, including ultra-small particles ($R = 1.3$ nm) with $\Delta E_{conf} \approx 700$ meV, ~40% of the bulk CdSe band gap[61].

Principles of CQD lasing

Optical-gain threshold. Key features of light amplification in strongly confined CQDs can be understood by approximating the lowest-energy emitting transition by a simple two-level system that contains two electrons of opposite spins in its valence band (VB) state (FIG. 2a, left). If one electron is promoted into the conduction band (CB), this generates a single e–h pair, an exciton. Such a state can emit light; however, it does not amplify incident photons, as the probability of stimulated emission by the CB electron is equal to that of photon absorption by the electron remaining in the VB.

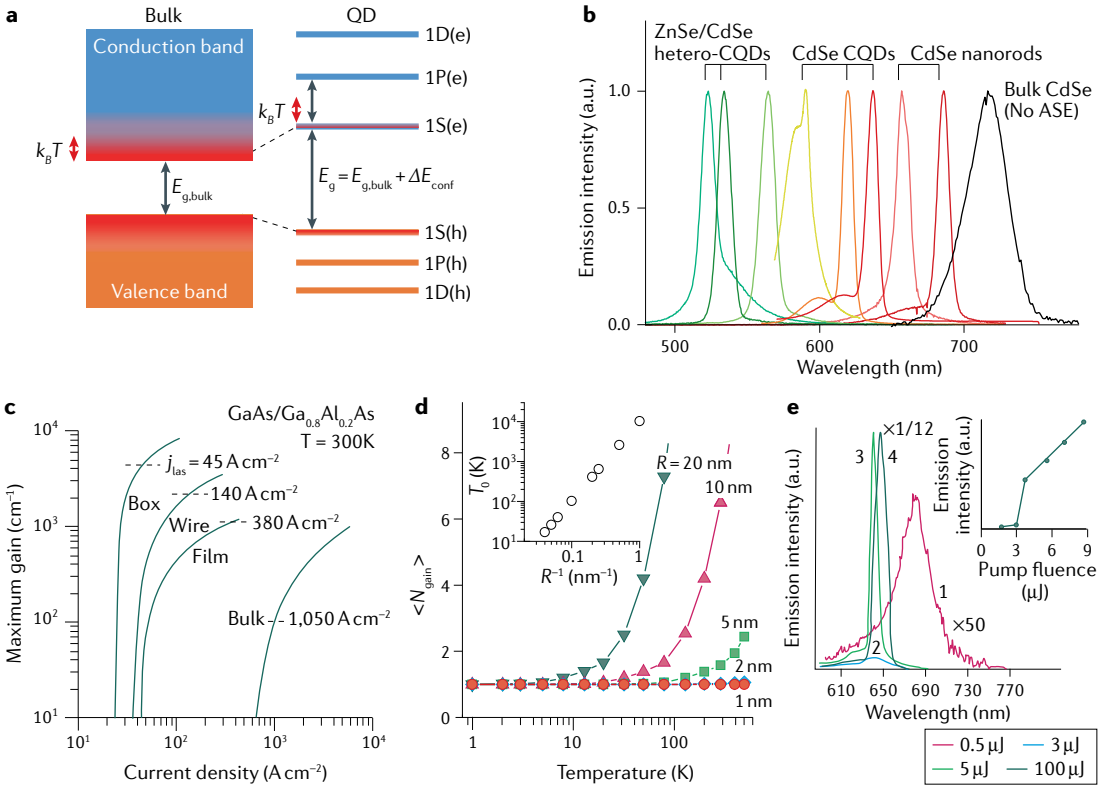

Fig. 1 | **Quantum dot lasing: from the theoretical concept to the practical demonstration. a** | Unlike bulk semiconductors, which have continuous conduction and valence energy bands, semiconductor quantum dots (QDs) feature discrete atomic-like states with energies that are determined by the QD radius *R*. This leads to a size-dependent band gap $E_g = E_{g,bulk} + \Delta E_{conf}$, where $E_{g,bulk}$ is the bulk band gap and ΔE_{conf} is a confinement energy that scales approximately as $1/R^2$. The three lowest energy levels, labelled as 1S, 1P and 1D, correspond to states with angular momenta 0, 1 and 2, respectively. The double-sided red arrow schematically represents the thermal energy k_BT, where k_B is the Boltzmann constant and *T* the temperature. In a bulk solid, many states reside within the k_BT interval, whereas in the QDs, k_BT is smaller than the inter-state spacing, which inhibits thermal depopulation of the band-edge 1S levels. **b** | The room-temperature amplified spontaneous emission (ASE) of colloidal CdSe-based nanostructures with varied sizes, shapes and internal structure shows spectral tunability from red to green[57]. The coloured traces show ASE spectra of CdSe colloidal QDs (CQDs) and nanorods, as well as ZnSe/CdSe core–shell nanostructures. These data were collected using 3.1-eV, 100-fs pulsed excitations. Due to thermal spreading of the electron and hole populations over the continuous band-edge states, bulk CdSe does not exhibit ASE under these excitation conditions (black line). **c** | Maximal optical gain versus injection current density calculated for GaAs-based 0D boxes (that is, QDs), 1D wires, 2D films (that is, quantum wells) and a bulk GaAs solid[59]. The lasing thresholds (j_{las}, marked by dashed lines) progressively decrease as the dimensionality is reduced from 3D (bulk) to 2D, 1D and, finally, 0D. **d** | Calculated optical-gain threshold, $\langle N_{gain} \rangle$, as a function of temperature for QDs with radii *R* from 1 to 20 nm. The inset shows the size dependence of the critical temperature T_0 (defined as the temperature at which $\langle N_{gain} \rangle = 2$). **e** | The first demonstration of QD lasing, performed using glass-embedded CdSe nanocrystals (~4-nm radius)[25]. When the sample, prepared as a Fabry–Pérot cavity, was excited with intense 20-ps, 2.33-eV pulses, it showed distinct signatures of lasing at *T* = 80 K, in particular, a sharp growth of the emission intensity with a clear threshold behaviour (inset). Spectra 1–4 were collected using pump pulses with energies of 0.5, 3, 5 and 100 μJ, respectively. Based on spectrum 3, which was recorded immediately above the lasing threshold, the energy of photons emitted in the lasing regime (~1.94 eV) was higher than the bulk CdSe band gap ($E_{g,bulk}$ = 1.83 eV at 80 K) by 110 meV, indicating a strong influence of the 0D confinement. Curve number 1 is multiplied by a factor of 50, curve number 4 by a factor of 1/12. e, electron; h, hole. Panel **b** is adapted with permission from REF.[57], ACS. Panel **c** is reproduced with permission from REF.[59], IEEE. Panel **e** is reproduced with permission from REF.[25], Springer.

This corresponds to the situation of 'optical transparency' or optical-gain threshold (FIG. 2a, middle). Only when the second VB electron is also excited to the CB can the CQD amplify light, implying that the population inversion, required for the lasing action, is realized only when at least a fraction of the CQDs in the sample is excited with two e–h pairs, or biexcitons (FIG. 2a, right).

The above considerations indicate that, in the case of a twofold degeneracy of electron and hole states ($g_e = g_h = 2$), the optical-gain threshold corresponds to the situation in which the average number of excitons per dot is 1. As we mentioned earlier, this condition can be obtained from the analysis of quasi-Fermi potentials. Indeed, if we assume that an individual CQD in the ensemble contains no more than 2 excitons, the average per-dot electron and hole occupancies ($\langle N_e \rangle$ and $\langle N_h \rangle$, respectively) can be related to ϕ_e and ϕ_h by $\langle N_{e,h} \rangle = g_{e,h} / [\exp(\phi_e / k_BT) + 1]$, where k_B is the Boltzmann constant

and T the temperature. In the case of charge-neutral dots ($\langle N_e \rangle = \langle N_h \rangle = \langle N \rangle$), this expression leads to the following condition for the gain threshold: $\phi_e + \phi_h = k_B T \ln[(g_e/\langle N_{gain} \rangle - 1)(g_h/\langle N_{gain} \rangle - 1)] = 0$ or $\langle N_{gain} \rangle = g_e g_h/(g_e + g_h)$. If $g_e = g_h = 2$, we obtain $\langle N_{gain} \rangle = 1$.

In practically realized CQDs, however, the band-edge state degeneracy can be greater than 2. For example, in II–VI CQDs, the VB levels are derived from the light and heavy hole states. If the splitting between these states (Δ_{lh}) is much smaller than $k_B T$, the hole-state degeneracy is 4, which increases $\langle N_{gain} \rangle$ to 4/3. In the opposite situation ($\Delta_{lh} \gg k_B T$), which is realized, for example, in asymmetrically strained CQDs[48,67], $\langle N_{gain} \rangle$ approaches its ideal value of 1.

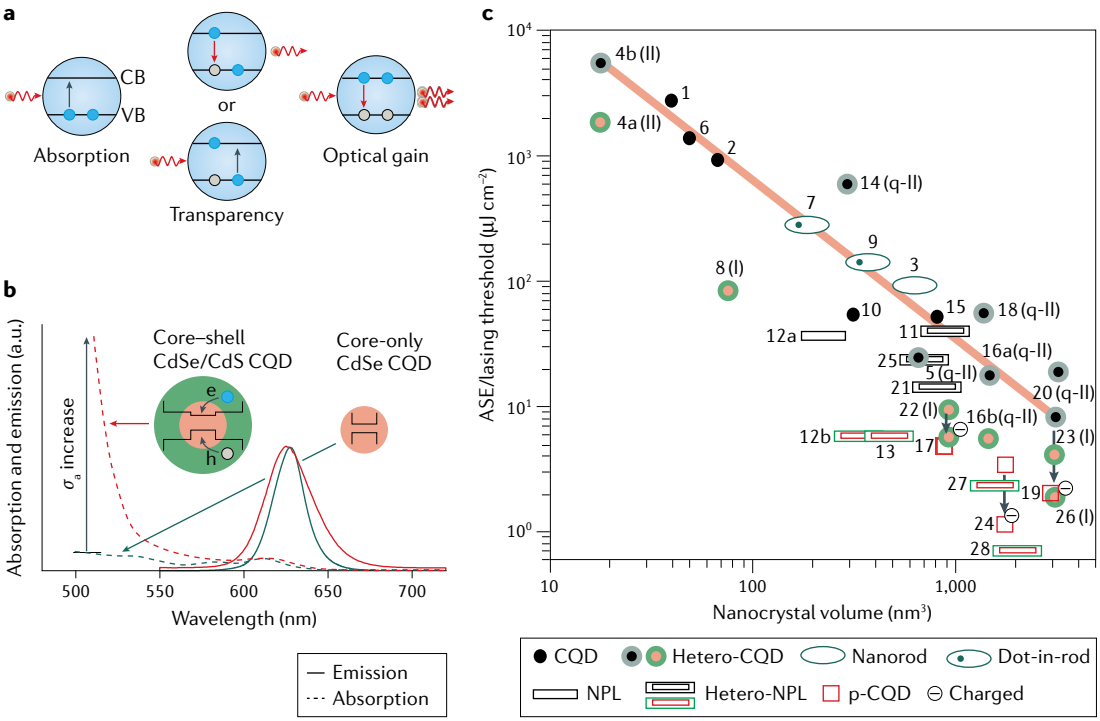

Fig. 2 | **Principles of colloidal quantum dot lasing and manipulation of amplified spontaneous emission/lasing thresholds via shape control and heterostructuring. a** | A simplified optical-gain model in which a colloidal quantum dot (CQD) band-edge transition is approximated by a two-level system comprised of twofold-degenerate valence band (VB) and conduction band (CB) states. In the ground state (left), both electrons residing in the VB state can absorb an incident photon (red wavy arrow). When one electron is promoted into the CB (single-exciton state), absorption by the remaining VB electron becomes balanced by stimulated emission produced by the CB electron; this corresponds to the state of 'transparency' or optical-gain threshold. When both electrons are excited into the CB (biexciton state), the absorption is completely eliminated and the incident photon can only induce stimulated emission; this corresponds to the regime of optical gain. **b** | In thick-shell CQD heterostructures, the shell of a wider-gap material serves as a light-harvesting antenna for the smaller-band-gap emitting core. This can be used to boost the absorption cross-section compared with core-only particles, while preserving the emission wavelength. Here, the effect of a thick shell is illustrated by comparing absorption (dashed lines) and emission (solid lines) spectra of core-only CdSe (blue) and 'giant' CdSe/CdS CQDs (red); the core radius is 1.5 nm and the shell thickness is 5.5 nm. The absorption spectra are normalized so as to match the 1S band-edge peak. This representation shows that, owing to the thick shell, the absorption cross-section (σ_a) at 500 nm is increased by a factor of 27 in the CdSe/CdS CQDs. **c** | A survey of amplified spontaneous emission (ASE)/lasing thresholds ($w_{las,ASE}$) plotted as a function of nanocrystal volume for spherical CQDs (solid black circles)[61,85–88], hetero-CQDs (concentric circles, black–grey or coloured) of type I (denoted I)[43,44,49,93], type II (denoted II)[91] and quasi-type II (denoted q-II)[1,70,89,90,92], nanorods (open ovals)[72], dot-in-rods (ovals with a dot inside)[73,74], nanoplatelets (NPLs, open rectangles)[76], hetero-NPLs (double rectangles, black or coloured)[75–81] and cube-shaped perovskite CQDs (p-CQDs, open squares)[82–84]. In most measurements, the samples were excited using short, 400-nm laser pulses. The exception is point 14, which was obtained using a 480-nm excitation[92]. Points 4a and 4b are single-exciton and biexciton ASE thresholds, respectively, measured for type II CdS/ZnSe CQDs[91] (the volume is calculated based on the core size because the ZnSe shell absorption at the excitation energy is negligible). Points 16a and 16b indicate the lasing thresholds observed for thick-shell 'giant' CdSe/CdS CQDs with an abrupt and a graded interface, respectively[90]. Points 12a and 12b are CdSe NPLs and CdSe/CdS hetero-NPLs[76], respectively. Points 22 and 26 correspond to sub-single-exciton ASE[44] and lasing[43], respectively, realized using negatively charged type I continuously graded CQDs. Point 24 is the ASE threshold measured for charged $CsPbBr_3$ p-CQDs[82]. This survey shows a systematic volume (V)-dependent trend: the ASE/lasing threshold decreases with increasing nanocrystal volume. The majority of the data points (shown in black and grey) can be approximately described by the dependence $w_{las,ASE} \propto V^{-1.25}$ (pink line). The 'outliers' below the trend line (coloured symbols) correspond to the reduced thresholds realized owing to either a nonstandard (that is, non-biexcitonic) gain mechanism or a special nanocrystal design optimized for lasing. Vertical arrows show the extent of reduction of $w_{las,ASE}$ due to charging or doping. e, electron; h, hole.

Thus, in the case of II–VI CQDs, the optical-gain threshold is between 1 and 4/3 excitons per dot, independent of the CQD size or shape. However, if the gain threshold is evaluated in terms of per-pulse pump fluence (w, pulsed excitation), it can widely vary from one structure to another, depending on the absorption cross-section (σ_a), as $w = \langle N \rangle h\nu_p/\sigma_a$, where $h\nu_p$ is the pump photon energy[68]. Because σ_a scales directly with the nanostructure volume[68,69], one approach to increase it, without lessening the confinement effects, is to enclose a small emitting core into a thick shell of a wider-gap material, which serves as a large light-harvesting antenna coupled to the quantum-confined emitter (FIG. 2b). This approach has been practically implemented using, for example, thick-shell 'giant' CdSe/CdS CQDs (g-CQDs)[70,71] and compositionally graded CdSe/$Cd_xZn_{1-x}Se$ core–shell structures[49].

Reduced optical-gain thresholds were also obtained with other types of large-volume nanocrystals, such as nanorods[72], dot-in-rod structures[73,74], NPLs[75–81] and perovskite CQDs (p-CQDs)[82–84]. In FIG. 2c, we plot the ASE and lasing thresholds ($w_{las,ASE}$) versus nanocrystal volume (V) for a large collection of nanostructures reported in the literature (all data are for short-pulse excitation). This plot indicates that the majority of the published data (black symbols; spherical CQDs[61,85–88], hetero-CQDs[1,43,70,89–92], nanorods[72], dot-in-rods[73,74], NPLs[76] and hetero-NPLs[75,78,79]) can be described by the simple power dependence $w_{las,ASE} \propto V^{-1.25}$ (pink line). This suggests that, in most cases, the reduced ASE/lasing thresholds were obtained through enhancement of absorption cross-sections. As described in later sections, a further reduction in $w_{las,ASE}$ can be obtained through advanced control of CQD properties (coloured symbols) via means such as impeded Auger recombination[43,44,49,90], single-exciton gain[81,91,93] and suppressed reabsorption realized by CQD charging[43,44,82].

Size-dependent trends in Auger recombination. As we showed earlier, optical-gain species in CQDs are biexciton states (FIG. 3a, left), which suggests that optical-gain dynamics are controlled not by single-exciton decay but by biexciton recombination. Even in the absence of defect-related nonradiative processes, the presence of multiple carriers in a CQD opens an intrinsic nonradiative pathway involving Auger recombination[66,94–97]. In this process, the e–h recombination energy does not produce a photon but, instead, is transferred to a third carrier (an electron or a hole), which, as a result, is excited to a higher-energy state within the same band (FIG. 3a, right). Nonradiative Auger decay directly competes with stimulated emission (FIG. 3a, left); therefore, understanding the interplay between these two effects is critical to CQD laser development.

In epitaxial QDs, Auger recombination is slower than radiative decay and does not represent a significant impediment for lasing. In sharp contrast, in standard (non-engineered) CQDs, the rates of Auger decay are extremely fast and exceed those of radiative decay by several orders of magnitude[66,94]. Signatures of very fast Auger recombination were initially revealed by studies of glass-embedded nanocrystals[98,99]. Detailed quantitative insights into the timescales of this process were obtained from follow-up studies of highly monodisperse, size-controlled colloidal samples[66]. In particular, these studies revealed a linear scaling of Auger lifetimes with the CQD volume. This trend, often referred to as V-scaling, is surprisingly general and is observed for nanocrystals of virtually all studied semiconductors, including CdSe, InAs, PbSe, PbS, Si and Ge[18,94,100–102]. In FIG. 3b, it is illustrated by several independent literature measurements of CdSe CQDs (open dark green symbols), all of which show remarkable consistency with the V-scaling trend[66,101,103–105]. Based on these observations, the biexciton Auger lifetime ($\tau_{A,XX}$) can be estimated from $\tau_{A,XX} = \chi V$, where χ is ~1 ps nm^{-3} (dark green line). One known exception is p-CQDs[106,107]. While they also follow a V-scaling trend (open blue symbols), their Auger lifetimes are more than ten times shorter than those of other materials and, therefore, χ is considerably smaller ($\chi = 0.06$ ps nm^{-3}, blue line). As discussed later in this Review, an important component of present-day CQD lasing research is Auger decay engineering, which encompasses approaches such as heterostructuring and compositional grading for extending Auger lifetimes beyond the values expected for V-scaling[47–50] (light green, purple and red symbols).

Very fast rates of Auger decay greatly reduce the emissivity of biexcitons. The quantum yield (QY) of biexciton photoluminescence (PL) can be calculated as $q_{XX} = \tau_{XX}/\tau_{r,XX} = \tau_{A,XX}/(\tau_{r,XX} + \tau_{A,XX})$, where $\tau_{r,XX}$ is the radiative biexciton lifetime and $\tau_{XX} = \tau_{r,XX}\tau_{A,XX}/(\tau_{r,XX} + \tau_{A,XX})$ the overall biexciton lifetime. To calculate the biexciton radiative lifetime, we apply statistical considerations[90,101,108]. If we denote the rate of a single spin-allowed CB–VB transition as γ, the total rate of the transition between the exciton state, $|X\rangle$, and the ground state, $|0\rangle$, is $\gamma/2$, as only 2 of 4 spin combinations comprising the $|X\rangle$ state are optically active[90] (FIG. 3c). Because both transitions that couple the biexciton state ($|XX\rangle$) to the single-exciton state are optically active, the corresponding rate is 2γ. Hence, the biexciton and the exciton ($\tau_{r,X}$) radiative lifetimes are connected by $\tau_{r,XX} = \tau_{r,X}/4$, which yields $q_{XX} = 4\tau_{XX}/\tau_{r,X}$, if we assume that single-exciton decay is purely radiative.

For our quantitative estimations, we use the example of CdSe CQDs, for which $\tau_{r,X} \approx 20$ ns (REF.[109]) and $\tau_{r,XX}$ is ~5 ns. Based on V-scaling, for CQDs with R from 1 to 4 nm (typical of standard CdSe particles), $\tau_{A,XX}$ is between ~4 and ~270 ps. Because $\tau_{r,XX}$ is much longer than $\tau_{A,XX}$, the biexciton decay is dominated by Auger recombination (that is, $\tau_{XX} \approx \tau_{A,XX}$) and, hence, $q_{XX} \approx 4\tau_{A,XX}/\tau_{r,X}$. Based on this expression, the size-dependent biexciton PL QY is in the range 0.1–5%, indicating that biexcitons are virtually nonemissive in small CQDs and become only weakly emissive in large particles. This represents a serious complication for lasing, as optical gain in CQDs is due to biexcitons (FIG. 3a).

Optical gain and Auger recombination. A direct connection between CQD gain and biexciton states was originally revealed in REF.[61], which also analysed the implications of nonradiative Auger recombination for CQD lasing and, in particular, established that this

process imposes a strict limit on a minimal (critical) concentration of CQDs ($\rho = \rho_{crit}$), below which ASE and lasing are impossible. This limit is defined by the condition that the maximal rate of stimulated emission τ_0^{-1} achievable for a given ρ is equal to the optical-decay rate due to Auger recombination, that is, $\tau_0^{-1} = \tau_{A,XX}^{-1}$. τ_0 can be found from $\tau_0 = \beta n/(cG_0)$, where c is the speed of light in vacuum, n is the refractive index, G_0 is the maximal (saturated) gain coefficient (G) realized when each CQD contains two or more excitons, and β is a dimensionless

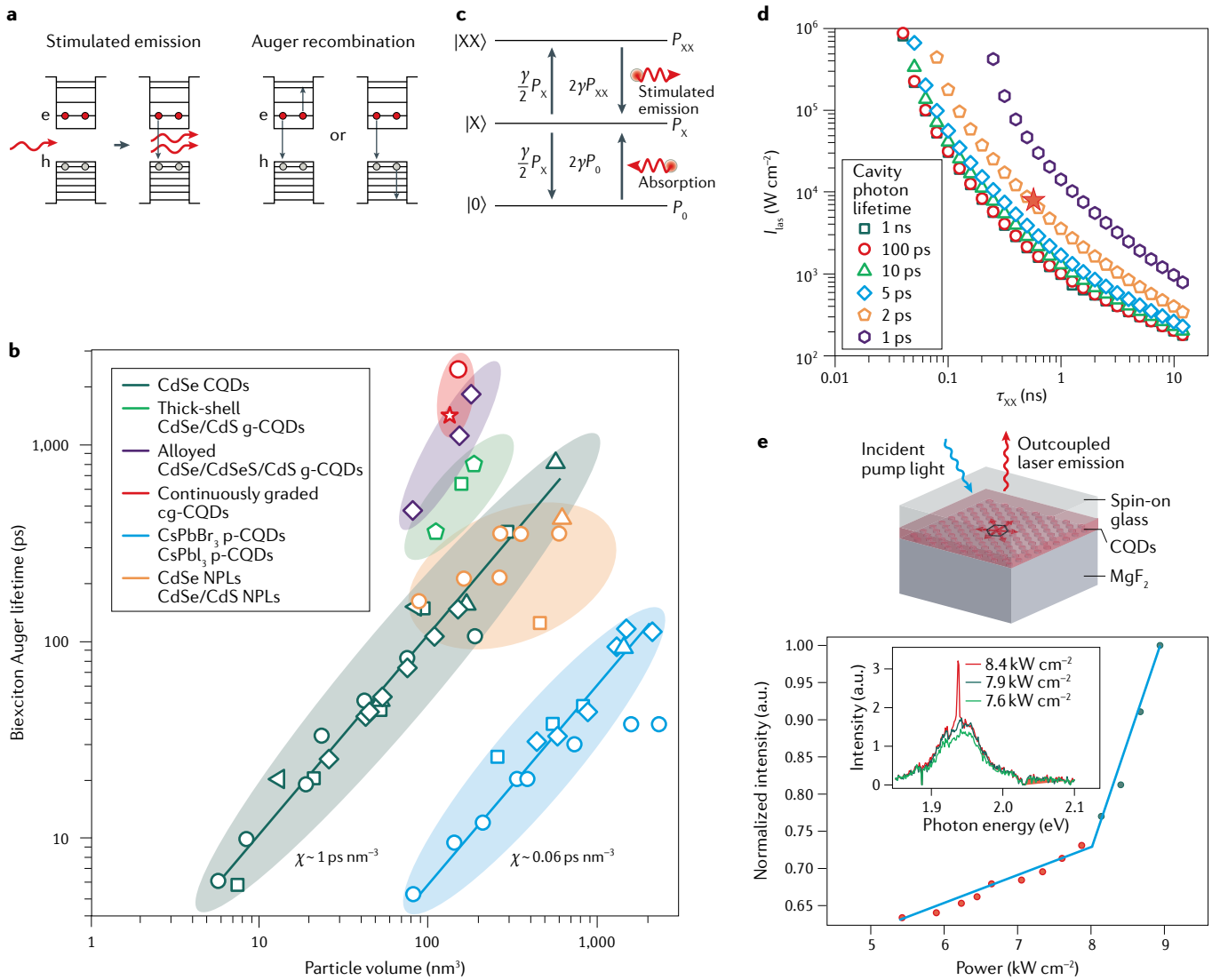

Fig. 3 | **Auger recombination and colloidal quantum dot lasing.** **a** | In colloidal quantum dots (CQDs), light amplification occurs owing to stimulated emission from biexcitons (left). This process competes with biexciton nonradiative decay via the Auger process (right). During Auger recombination, the electron–hole recombination energy is transferred to either an electron or a hole residing in the same dot. **b** | The dependence of biexciton Auger lifetimes, $\tau_{A,XX}$, on particle volume, V, for different types of colloidal nanocrystals, including CdSe CQDs (dark green squares[66], circles[105], diamonds[103] and triangles pointing left[101] and up[104]), thick-shell CdSe/CdS 'giant' CQDs (g-CQDs, light green pentagons[47] and square[48]), single-step-alloyed CdSe/$CdSe_{0.5}S_{0.5}$/CdS CQDs (purple diamonds[47]), continuously graded (cg) CdSe/$Cd_xZn_{1-x}Se$/$ZnSe_{0.5}S_{0.5}$ cg-CQDs (red circle[49] and star[50]), perovskite CQDs (p-CQDs, blue squares[106], circles[107], up-pointing triangle[106] and diamonds[107]), CdSe nanoplatelets (NPLs, orange square[77] and circles[102]) and CdSe/CdS NPLs (orange up-pointing triangle[76]). The lines are fits to a linear dependence ($\tau_{A,XX} = \chi V$), which yield $\chi \approx 1$ ps nm^{-3} for CdSe CQDs and 0.06 ps nm^{-3} for p-CQDs. **c** | A 'truncated-energy-spectrum' model of optical gain in CQDs[90]. It considers three states of direct relevance to light amplification: the ground state, $|0\rangle$, the exciton state, $|X\rangle$, and the biexciton state, $|XX\rangle$. Their occupation probabilities are P_0, P_X and P_{XX}, respectively. The rates of absorbing and emitting transitions shown, respectively, by arrows pointing upwards and downwards, are indicated. γ is the rate of a single, spin-conserving transition. **d** | Modelling of the continuous-wave (cw) lasing threshold (I_{las}) as a function of the total biexciton lifetime (τ_{XX}) due to both radiative and nonradiative Auger decay[90]. The biexciton radiative decay time was fixed ($\tau_{r,XX} = 12.5$ ns), while the Auger lifetime ($\tau_{A,XX}$) was varied from 40 ps to ∞. The different symbols correspond to different cavity photon lifetimes (τ_c). The red star indicates the cw lasing threshold realized in REF.[48] for thick-shell CdSe/CdS CQDs with $\tau_{XX} \approx 600$ ps. **e** | A schematic depiction of a lasing device[48] composed of thick-shell, biaxially strained CdSe/CdS CQDs coupled to a 2D photonic crystal cavity (top). Normalized surface-emission intensity as a function of intensity of a cw laser used as a pump source (2.81-eV photon energy, bottom). A sharp increase in the emitted-light intensity indicates a transition to lasing, which occurs at ~8 kW cm^{-2} (REF.[48]). Inset: the spectra of surface-emitted light recorded as a function of pump intensity show a narrow lasing line above the lasing threshold. Panels **c** and **d** are adapted with permission from REF.[90], ACS. Panel **e** is reproduced with permission from REF.[48], Springer Nature Limited.

constant defined by the parameters of a coupled CQD–optical cavity system[61,90]. Because G_0 is directly proportional to ρ ($G_0 = 2\gamma\rho n/c$)[90], τ_0 scales inversely with the CQD concentration: $\tau_0 = \beta/(2\gamma\rho)$. This leads to the following condition for the critical CQD density: $\beta/(2\gamma\rho_{crit}) = \tau_{A,XX}$ or $\rho_{crit} = \beta/(2\gamma\tau_{A,XX})$. If we express ρ_{crit} in terms of the volume fraction of CQD semiconductor cores in the gain medium ($\xi_{crit} = \rho_{crit}V$), the critical condition can be presented as $\xi_{crit} = V\beta/(2\gamma\tau_{A,XX})$ or $\xi_{crit} = \beta/(2\gamma\chi)$ if we assume that $\tau_{A,XX}$ exhibits standard V-scaling.

To estimate ξ_{crit}, we use $\beta/(2\gamma) \approx 0.02\,ps\,nm^{-3}$ (REF.[90]) and $\chi \approx 1\,ps\,nm^{-3}$, which yields $\xi_{crit} \approx 2\%$. Although 2% is a fairly modest amount of active semiconductor material, owing to solubility limits, it is not readily accessible in CQD solutions. This explains the failure of earlier efforts to obtain CQD lasing using liquid-dye-like laser configurations and emphasizes the need for a dense CQD medium for attaining ASE and lasing effects. In REF.[61], the required CQD density was achieved using close-packed film samples, wherein ξ was >15%. By applying short-pulse excitation ($\tau_p = 100\,fs$) to minimize Auger losses during the pumping stage, the authors of this report were able to demonstrate ASE, which proved the feasibility of lasing with colloidal nanomaterials. Indeed, shortly after, a true lasing action was realized using CQDs coupled to various types of optical cavities[85,110–112]. However, Auger recombination continues to represent a major obstacle for the realization of practical CQD lasers. Therefore, Auger decay engineering has been a focus of recent lasing-related research.

Effect of Auger decay on optical-gain thresholds. To quantitatively analyse the implications of fast Auger recombination for CQD lasing, the authors of REF.[90] introduced a truncated-energy-spectrum model, which includes three states of direct relevance to light amplification: $|0\rangle$, $|X\rangle$ and $|XX\rangle$ (FIG. 3c). Because their occupation probabilities are connected by $P_0 + P_X + P_{XX} = 1$, the average 'truncated' per-dot occupancy, $\langle N^* \rangle = P_X + 2P_{XX}$, is automatically limited to 2. To apply this model to experimental measurements, where $\langle N \rangle$ can be greater than 2, one can relate model probabilities P_j ($j = 0$, X, XX) to actual CQD occupation probabilities, p_i ($i = 0, 1, \ldots \infty$), by $P_0 = p_0$, $P_X = p_1$ and $P_{XX} = \Sigma_{i=2}^{\infty} p_i = 1 - p_0 - p_1$ (summation is because, if $g_e = g_h = 2$, multiexcitons with $i > 2$ contribute to the band-edge gain in the same way as a biexciton).

Using the above model, the optical-gain coefficient of a CQD medium can be presented in terms of the difference of per-dot rates of stimulated emission ($r_e = 2\gamma P_{XX} + \gamma P_X/2$) and absorption ($r_a = 2\gamma P_0 + \gamma P_X/2$, FIG. 3c): $G = \rho nc^{-1}(r_e - r_a) = G_0(P_{XX} - P_0)$, where G_0 is the saturated gain coefficient realized when $P_{XX} = 1$ (REF.[90]). In regard to a standard description of a lasing effect, $P_{inv} = P_{XX} - P_0$ represents the population inversion, which is defined as the difference in occupancies of the higher-energy and lower-energy states involved in light amplification. In CQDs, these two states are $|XX\rangle$ and $|0\rangle$ (FIG. 3c).

Based on the above model, the gain threshold corresponds to the condition $P_{inv} = P_{XX} - P_0 = 0$, which yields $\langle N^*_{gain} \rangle = 1$. In the case of pulsed excitation, when probabilities p_i can be described by the Poisson distribution[68], the truncated and true CQD occupancies are connected by $\langle N^* \rangle = 2 - e^{-\langle N \rangle}(2 + \langle N \rangle)$, which yields for the true gain threshold $\langle N_{gain} \rangle \approx 1.15$ or $w_g = 1.15h\nu_p/\sigma_a$ in terms of per-pulse fluence[90]. So, in the short-pump-pulse case ($\tau_p \ll \tau_{A,XX}$), Auger decay does not directly influence the optical-gain threshold. As a result, w_g is defined primarily by the absorption cross-section. This explains the general trend of direct scaling of pulsed ASE and lasing thresholds with the nanostructure volume (FIG. 2c), as σ_a is directly linked to V. However, even in this case, Auger recombination is still of crucial importance because, as discussed earlier, its timescale defines the minimal CQD density required to attain ASE and lasing.

To analyse the cw pumping case, we assume that a three-level system (FIG. 3c) is exposed to excitation with a constant per-dot rate g that induces the upward $|0\rangle$–$|X\rangle$ and $|X\rangle$–$|XX\rangle$ transitions. If we neglect the effects of stimulated emission (pre-lasing regime), the downward transitions between the same states occur due to spontaneous exciton and biexciton decay with rates $1/\tau_X$ and $1/\tau_{XX}$, respectively. Under the steady-state condition, the upward and downward flows of excitations balance each other. Specifically, $P_{XX}/\tau_{XX} = gP_X$ and $P_X/\tau_X = gP_0$, which yields $P_{XX} = g^2\tau_{XX}\tau_X P_0$. When combined with a standard optical-gain-threshold condition ($P_{XX} = P_0$), this leads to $g_{gain} = (\tau_{XX}\tau_X)^{-1/2}$ or $I_{gain} = (h\nu_p/\sigma_a)(\tau_{XX}\tau_X)^{-1/2}$ if the cw gain threshold is presented in terms of a pump intensity, $I = h\nu_p g/\sigma_a$.

The derived expressions indicate that, in the case of cw excitation, the gain threshold becomes explicitly dependent on exciton and biexciton lifetimes. In the radiative limit, $\tau_{XX} = \tau_X/4$ and $I^{rad}_{gain} = 2(h\nu_p/\tau_X\sigma_a)$. By contrast, in the case of fast Auger recombination ($\tau_{XX} \approx \tau_{A,XX}$), $I^{A}_{gain} = (h\nu_p/\sigma_a)(\tau_{A,XX}\tau_X)^{-1/2}$. The ratio of the two thresholds is $I^{A}_{gain}/I^{rad}_{gain} = 0.5(\tau_X/\tau_{A,XX})^{1/2}$ or $I^{A}_{gain}/I^{rad}_{gain} = (q_{XX})^{-1/2}$. This indicates that the effectiveness of cw pumping progressively diminishes with increased Auger recombination rate or, correspondingly, with decreased biexciton PL QY. This greatly complicates achieving the optical-gain regime in small-size CQD samples with short Auger lifetimes. For example, in the case of green-emitting CdSe CQDs with R of ~1.5 nm, $\tau_{A,XX}$ is ~15 ps (FIG. 3b) and q_{XX} is ~0.3% (for $\tau_X \approx 20$ ns (REF.[109])). This yields $I^{A}_{gain}/I^{rad}_{gain} \approx 18$. Thus, due to the influence of intrinsic Auger recombination, the cw optical-gain threshold is almost 20 times that of the purely radiative case.

Effect of Auger recombination on lasing thresholds. In comparison to gain thresholds, fast Auger recombination has an even stronger effect on cw lasing thresholds, as, in this case, stimulated emission by biexcitons must outcompete not only reabsorption by the gain medium (this defines the gain threshold) but also losses due to photon escape from the lasing cavity. To evaluate the effect of Auger decay and cavity losses on the lasing threshold, a coupled CQD–cavity system was studied[90], wherein the CQD was modelled using the three-level representation of FIG. 3c. According to the calculations conducted for the pulse-excitation regime, the population inversion required to achieve the lasing threshold ($P_{inv,las}$) depends, in general, on both the cavity photon lifetime (τ_c) and the biexciton Auger lifetime. However,

in the limit of a lossless cavity ($\tau_c \to \infty$), $P_{inv,las}$ is only a function of τ_{XX}: $P_{inv,las} = (\tau_0/\tau_{XX})^{1/2}$. Correspondingly, the lasing threshold is $\langle N^*_{las}\rangle = 1 + P_{inv,las} = 1 + (\tau_0/\tau_{XX})^{1/2}$, or $\langle N^*_{las}\rangle = 1 + (\tau_0/\tau_{A,XX})^{1/2}$ in the case of fast Auger recombination.

Unlike the gain threshold, which is insensitive to Auger decay, the lasing threshold in the pulsed-excitation case depends explicitly on $\tau_{A,XX}$. This is a direct consequence of the distinct timescales that characterize the development of optical-gain and lasing regimes. The state of the CQD-medium transparency (that is, optical-gain threshold) is reached immediately following the excitation. Therefore, the rate of Auger decay is irrelevant, as long as $\tau_p \ll \tau_{A,XX}$. By contrast, the development of lasing is not instantaneous but is characterized by a non-zero time constant (τ_{las}) that scales approximately inversely with the rate of stimulated emission. For lasing to occur, τ_{las} must be shorter than $\tau_{A,XX}$. Therefore, if $\tau_{A,XX}$ is decreased, the realization of lasing will require higher stimulated emission rates and, hence, greater $P_{inv,las}$.

The influence of Auger recombination is further enhanced in the case of cw pumping. The cw lasing threshold (I_{las}) can be estimated based on the pulsed lasing threshold (w_{las}) from $I_{las} = w_{las}/\tau_{gain}$, where τ_{gain} is the optical-gain lifetime. In standard CQDs, τ_{gain} is on the order of $\tau_{A,XX}$, therefore, $I_{las} \approx w_{las}/\tau_{A,XX}$. This indicates that, in the case of cw pumping, the dependence of the lasing threshold on Auger lifetime is amplified compared with the pulsed case due to the addition of the $1/\tau_{A,XX}$ scaling factor.

In FIG. 3d, we display the results of a numerical analysis of I_{las} versus τ_{XX} for CdSe CQDs[90]. These calculations indicate that I_{las} rapidly increases with decreasing biexciton lifetime. In particular, for $\tau_{XX} < 50$ ps, typical of medium and small dots ($R < 2$ nm), I_{las} is >1 MW cm^{-2}, which is well above the maximal intensities CQDs can withstand without damage[113]. To reduce I_{las} to levels below 10 kW cm^{-2}, which are compatible with colloidal nanomaterials[48], the biexciton lifetime must be increased to 500 ps or longer. This is possible with larger ($R > 5$ nm) monocomponent CQDs or large heterostructures (FIG. 3b).

Long Auger lifetimes of thick-shell g-CdSe/CdS structures were exploited to realize cw lasing in devices based on 2D photonic resonators[48] (FIG. 3e). The observed thresholds, $I_{las} = 6.4 - 8.4$ kW cm^{-2}, were consistent with the results of calculations presented in FIG. 3d (red star). This reaffirmed the conclusion of REF.[90] that the primary factor controlling cw lasing thresholds in CQD gain media is the biexciton lifetime. While providing long-awaited proof of feasibility of cw CQD lasers, the devices presented in REF.[48] showed limited stability and failed within 10–30 min, due likely to thermally induced degradation of the CQD gain medium. This indicates that a more complete suppression of Auger decay is required to further lower I_{las} and, thereby, achieve long-term stability of CQDs during cw laser operation.

Control of CQD properties for lasing

Manipulation of Auger lifetimes. Recent experimental studies demonstrate[47,49,67,114] that strong suppression of Auger decay is possible through control of the shape of the CQD confinement potential. In contrast to size control, for which lengthening of Auger lifetimes is accompanied by an unwanted reduction of the confinement energy, this approach allows for considerable suppression of Auger recombination while still preserving strong quantum confinement.

As was originally proposed in REF.[45], by 'smoothening' the potential-energy profile, one can reduce the rate of an intra-band transition involving an energy-accepting Auger electron (or hole, FIG. 3a, right) and, thereby, impede Auger recombination. Experimentally, an appreciable effect of the shape of the confinement potential on Auger decay was first observed for g-CdSe/CdS CQDs, wherein unintentional alloying of the core–shell interface led to the formation of a graded $CdSe_{1-x}S_x$ interlayer[70,115]. A more controlled suppression of Auger recombination was later achieved through intentional grading of the CQD composition. Initially, the effectiveness of this approach was demonstrated by incorporating a thin layer of $CdSe_{0.5}S_{0.5}$ alloy at the core–shell interface of g-CdSe/CdS CQDs[47,90]. Follow-up efforts explored CdSe/CdS CQDs with discrete multistep grading of the core–shell interface[114] and, more recently, continuously graded structures (cg-CQDs) implemented using a $CdSe/Cd_xZn_{1-x}Se$ system[49,67] (FIG. 4a).

In particular, using the cg-CQD approach, biexciton Auger lifetimes were extended to >2 ns ($\tau_{A,XX}$ was up to 2.4 ns, red circle in FIG. 3b) and, thereby, the biexciton emission QY was boosted to ~45%[49]. Importantly, the cg-CQDs still exhibited a large confinement energy of >250 meV. For comparison, standard CdSe CQDs with $\Delta E_{conf} = 250$ meV exhibit $\tau_{A,XX}$ of ~100 ps and q_{XX} of only ~2%.

Manipulation of optical-gain and lasing thresholds by CQD charging. The availability of CQDs with strongly suppressed Auger recombination opened up interesting opportunities for exploring novel gain mechanisms that rely not on neutral but charged excitations, which, in standard CQDs, would quickly decay via the Auger process. In particular, by charging (doping) CQDs with electrons or holes, it is possible to reduce (or to 'bleach') ground-state absorption and, thereby, lower the optical-gain threshold below the fundamental one-exciton limit[43,44,116] (FIG. 4b). In the case of complete bleaching of the band-edge transition, the condition for optical-gain threshold (that is, optical transparency) is realized without external excitation, which corresponds to the regime of 'zero-threshold' optical gain[44].

To obtain a quantitative relationship between the degree of CQD charging and the optical-gain threshold, we assume that each dot in the ensemble contains n_e permanent electrons. If such a charged sample is exposed to steady-state excitation, which generates $\langle N\rangle$ excitons per dot, the total average per-dot number of electrons is $\langle N_e\rangle = \langle N\rangle + n_e$. In this case, the electron quasi-Fermi potential can be presented as $\phi_e = k_B T \ln[g_e/(\langle N\rangle + n_e) - 1]$, while ϕ_h remains the same as for charge-neutral CQDs. Inserting ϕ_e and ϕ_h in the standard optical-gain condition ($\phi_e + \phi_h = 0$), we obtain $\langle N_{gain}\rangle = g_h(g_e - n_e)/(g_e + g_h)$.

The above expression indicates that the effect of permanent charges can be interpreted in terms of an effective reduction of the degeneracy of one of the band-edge

states (in our case, CB) involved in the lasing transition. This makes it easier to achieve band-edge optical transparency, which translates into reduced gain threshold. For example, in the case of singly charged CQDs ($n_e = 1$) with twofold degenerate band-edge states ($g_e = g_h = 2$), the gain threshold drops to $\langle N_{gain} \rangle = 0.5$ (FIG. 4b), implying that it can be realized by exciting only half of the CQD ensemble with a single exciton, thus, forming a charged exciton or a 'trion'. In the case of two injected charges, $\langle N_{gain} \rangle$ becomes zero, which corresponds to zero-threshold optical gain[44] (FIG. 4b).

Previous research into bulk semiconductor lasers explored doping as a means for reducing lasing thresholds[117,118]. However, these efforts encountered serious obstacles due to deleterious effects of fast Auger recombination. Recent progress in the development of CQDs with strongly suppressed Auger decay has opened interesting opportunities for practically exploiting the ideas of charged-exciton gain with colloidal nanostructures. Initial indications of the benefits of permanent charging for CQD optical-gain properties were obtained using electrochemical experiments with standard CdSe CQDs[116]. More recent efforts explored manipulation of optical gain via electrochemical doping of CdSe/CdS/ZnS heterostructures[119], as well as photochemical doping of specially engineered hetero-CQDs with either discrete or continuous alloying[43,44].

Studies of charged-exciton lasing[43] took advantage of considerable suppression of Auger recombination in CdSe/$Cd_xZn_{1-x}Se$/$ZnSe_{0.5}S_{0.5}$/ZnS cg-CQDs, which was especially strong for negatively charged excitons that served as optical-gain-active species. In particular, the PL QYs of singly (q_{X^-}) and doubly ($q_{X^{2-}}$) charged excitons were, respectively, 60% and 33% versus $q_{X^-} = 10\%$

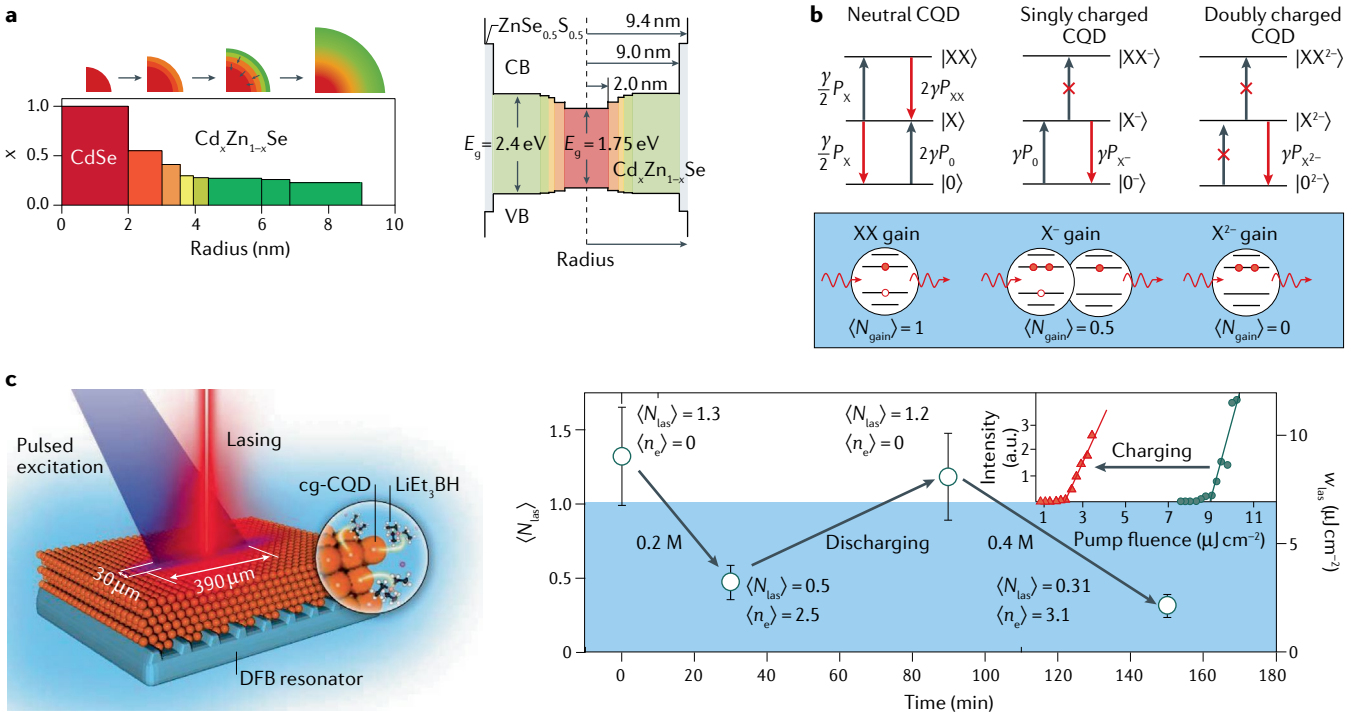

Fig. 4 | **Auger decay engineering and sub-single-exciton lasing using charged colloidal quantum dots. a** | Radial compositional profile of a continuously graded colloidal quantum dot (cg-CQD) comprising a 2-nm-radius CdSe core followed by a 7-nm compositionally graded $Cd_xZn_{1-x}Se$ shell[49] (left). Approximate profiles of the resulting conduction band (CB) and valence band (VB) confinement potentials (right). **b** | Optical-gain model for neutral and charged CQDs[43]. In neutral CQDs, optical gain is due to stimulated emission from biexcitons, which competes with ground-state $|0\rangle$–$|X\rangle$ absorption. The average number of excitons per dot needed to attain optical-gain threshold is $\langle N_{gain} \rangle = 1$: in this state, the two processes balance each other. In singly negatively charged CQDs, the absorbing transition from the charged exciton $|X^-\rangle$ (trion) to the charged biexciton $|XX^-\rangle$ is blocked, as the band-edge CB state is already occupied with two electrons. Therefore, gain is possible due to stimulated emission from trions that competes with partially suppressed ground-state absorption. In this case, the gain-threshold condition corresponds to the situation in which half of the dots are excited with trions and half remain in the charged ground state; that is, $\langle N_{gain} \rangle = 0.5$. In doubly negatively charged CQDs, both absorbing transitions ($|0^{2-}\rangle$–$|X^{2-}\rangle$ and $|X^{2-}\rangle$–$|XX^{2-}\rangle$) are blocked, therefore, optical amplification can occur with an arbitrarily small number of doubly charged single excitons. This corresponds to 'zero-threshold' optical gain ($\langle N_{gain} \rangle = 0$). **c** | A schematic depiction of the set-up used in REF.[43] to study charged-exciton lasing (left). A device made of cg-CQDs assembled on top of a second-order distributed feedback (DFB) resonator is immersed into tetrahydrofuran. To photochemically charge CQDs with extra electrons, controlled amounts of a photoreductant ($LiEt_3BH$) are added to tetrahydrofuran. The devices are excited using 400-nm, 130-fs laser pulses. Measurements of the effect of charging on lasing thresholds are shown on the right[43]. In neutral cg-CQDs, the average number of excitons per dot needed to observe lasing, $\langle N_{las} \rangle$, is 1.3. The threshold drops to $\langle N_{las} \rangle = 0.5$ upon 30-min exposure to 0.2 M $LiEt_3BH$ ($\langle n_e \rangle = 2.5$). After the cg-CQDs are discharged, $\langle N_{las} \rangle$ recovers its near original value of 1.2. A subsequent charging with 0.4 M $LiEt_3BH$ ($\langle n_e \rangle = 3.1$) leads to a stronger drop of the lasing threshold, which becomes only 0.31 excitons per dot on average. The blue shading highlights the area corresponding to sub-single-exciton lasing thresholds. Inset: the plot of the surface emission intensity versus pump fluence illustrates a more than fourfold reduction of the lasing threshold upon charging. Panel **a** is adapted with permission from REF.[49], Springer Nature Limited. Panels **b** and **c** are adapted with permission from REF.[43], AAAS.

and $q_{X^{2-}} = 3.5\%$ for standard CdSe CQDs with the same band gap. Further, the lifetimes of both charged excitons ($\tau_{X^-} = 4.5$ ns and $\tau_{X^{2-}} = 2.5$ ns) in the cg-CQDs were longer than that of a neutral biexciton ($\tau_{XX} = 1.5$ ns). As a result, charged-exciton gain relaxed considerably more slowly than biexciton gain and, importantly, it persisted for a few nanoseconds, that is, long after the biexciton gain had completely decayed.

Benefits of the charging approach were evident upon direct comparison of the lasing performance of neutral and charged cg-CQDs[43]. Lasing devices were prepared by depositing a film of cross-linked CdSe/$Cd_xZn_{1-x}Se$/$ZnSe_{0.5}S_{0.5}$/ZnS cg-CQDs on top of a distributed feedback (DFB) resonator (FIG. 4c, left). These structures were immersed into tetrahydrofuran (THF) and excited with 3-eV, 130-fs pulses. In pristine THF, the lasing threshold was ~9 μJ cm^{-2}, which corresponds to $\langle N_{las} \rangle = 1.3$ (±0.3), in line with the estimated neutral-CQD gain threshold of ~1.2 (REF.[43]) (FIG. 4c, right). To initiate CQD charging, lithium triethylborohydride ($LiEt_3BH$), which acted as a photoreductant[120], was added to THF. For 0.4 M $LiEt_3BH$, the average per-dot number of photoinjected electrons, $\langle n_e \rangle$, was ~3, which was sufficient to completely bleach the band-edge transition and, thereby, realize zero-threshold optical gain[44]. The benefits of this regime were apparent in a dramatic, ~fourfold reduction of the lasing threshold compared with neutral CQDs (FIG. 4c, inset). In this case, the onset of the lasing regime occurred at 2.1 μJ cm^{-2}, corresponding to just 0.31 (±0.07) excitons per dot, on average. This demonstrates the practical utility of charged-exciton gain for realizing ultra-low, sub-single-exciton lasing thresholds.

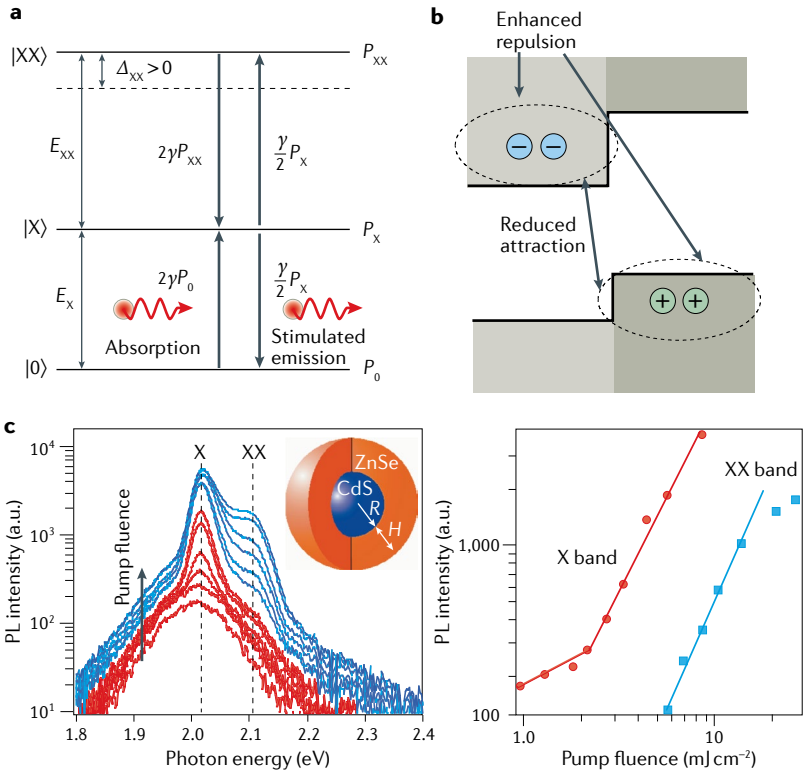

Fig. 5 | **Single-exciton gain using engineered exciton–exciton repulsion.** **a** | A 'truncated-energy-spectrum' model modified to account for the exciton–exciton (X–X) interaction, which shifts the absorbing |X⟩–|XX⟩ transition versus the emitting |X⟩–|0⟩ transition. If the energy of this interaction (Δ_{XX}) is sufficiently large and repulsive ($\Delta_{XX} > 0$), optical gain becomes possible with single excitons. **b** | The strong X–X repulsion needed to practically implement single-exciton gain can be realized using type II heterostructures, which favour co-localization of same-sign charges in the same part of the hetero-nanocrystals and separation of charges of opposite sign across the interfaces. This type of localization enhances the repulsive component of the Coulomb interaction and decreases its attractive component. The net effect is the development of strong X–X repulsion[122]. **c** | The pump-fluence-dependent emission spectra (left) of type II CdS/ZnSe colloidal quantum dots (shown in the inset; $R = 1.6$ nm, $H = 2$ nm) exhibit an amplified spontaneous emission (ASE) peak emerging near the centre of the single-exciton band (~2.01 eV). The second ASE feature (~2.11 eV), which develops at higher fluences, is shifted to higher energies versus the single-exciton line by ~100 meV, which is consistent with the energy of biexciton emission inferred from transient photoluminescence (PL) measurements[91]. The PL intensity as a function of pump fluence (right) indicates that the transition to the ASE regime occurs at ~2 mJ cm^{-2} for single excitons and ~6 mJ cm^{-2} for biexcitons[91]. These data were collected using 200-fs, 3-eV pulsed excitation with fluences of 1–30 mJ cm^{-2}. |0⟩, ground state; |X⟩, exciton state; |XX⟩, biexciton state; γ, rate of a single spin-conserving transition; E_{XX} and E_X, transition energies for the |X⟩–|XX⟩ and |X⟩–|0⟩ transitions, respectively; P_0, P_X and P_{XX}, occupation probabilities of |0⟩, |X⟩ and |XX⟩, respectively. Panel **b** is adapted with permission from REF.[122], ACS. Panel **c** is reproduced with permission from REF.[91], Springer Nature Limited.

Single-exciton optical gain. Another demonstrated approach for lowering the optical-gain threshold via the reduction of degeneracy of the band-edge levels is based on the manipulation of exciton–exciton (X–X) interactions[91,121,122]. In particular, it utilizes engineered, strong X–X repulsion to upshift the absorbing |X⟩–|XX⟩ transition versus the emitting |X⟩–|0⟩ transition (transition energies are E_{XX} and E_X, respectively)[91,121,122] (FIG. 5a). If the energy of the X–X interaction ($\Delta_{XX} = E_{XX} - E_X$) is greater than the transition linewidth (Γ), the |X⟩–|XX⟩ absorption ceases to interfere with the |X⟩–|0⟩ stimulated emission, implying that gain can occur with single excitons. Importantly, not only does this single-exciton scheme lower the optical-gain threshold, but it also eliminates the problem of fast Auger recombination, as light amplification occurs without the participation of biexcitons.

In standard CQDs, the X–X interaction is attractive ($\Delta_{XX} < 0$)[105,123], therefore, the realization of X–X repulsion ($\Delta_{XX} > 0$) requires specially engineered nanostructures. In addition to having the 'correct' sign, Δ_{XX} should also be sufficiently large, as the magnitude of the X–X interaction energy must exceed an ensemble (that is, inhomogeneous) emission linewidth. This implies that the practical realization of single-exciton gain is simplified for more monodisperse samples with a narrower Γ.

It is possible to switch the sign of Δ_{XX} using type II heterostructures, wherein a staggered band alignment creates an energy gradient that separates an electron and a hole between distinct regions of the structure[121] (FIG. 5b). In the case of a biexciton state, this enhances repulsion by favouring co-localization of charges of the same sign. Simultaneously, it decreases Coulombic attraction, as the charges of opposite sign are separated across the heterointerface. The net effect is 'giant' X–X repulsion, which, in small-size CQDs, can reach energies greater than 100 meV (REFS[91,124]). This is sufficient to satisfy the condition of $|\Delta_{XX}| > \Gamma$, even in the case of a large inhomogeneous linewidth caused by CQD size polydispersity.

The idea of single-exciton optical gain and the scheme for its realization through strong X–X repulsion were originally introduced in REF.[121]. This study also provided initial experimental evidence for light amplification due to single excitons using CdSe/ZnSe CQDs that exhibited partial separation between electron and hole wavefunctions (quasi-type II localization). A few years later, ASE due to single excitons was unambiguously demonstrated using specially designed type II core–shell CdS/ZnSe CQDs (inset of FIG. 5c) that featured a giant Δ_{XX} of ~100 meV (REF.[91]). In particular, these samples displayed two ASE bands that developed one after another with increasing pump level (FIG. 5c). The first of these bands, located near the centre of spontaneous PL, was due to single-exciton gain. The second feature was due to usual biexcitonic gain; however, because of giant X–X repulsion, it was situated not on the red side of single-exciton emission (as in standard CQDs) but on its blue side (FIG. 5c, left). Following these proof-of-principle studies, single-exciton gain was realized with other types of CQDs[82,125] and, in particular, it was employed to demonstrate low-threshold, spectrally tunable, vertical-cavity surface-emitting lasers[93] (point 8 in FIG. 2c).

For the quantitative analysis of single-exciton gain, we consider the model of FIG. 5a. Assuming that $|\Delta_{XX}|$ is greater than Γ, we can neglect the biexcitonic $|X\rangle$–$|XX\rangle$ transition and calculate the single-exciton-gain magnitude from the difference of rates of the $|X\rangle$–$|0\rangle$ stimulated emission ($r_e = \gamma P_X$) and the $|0\rangle$–$|X\rangle$ absorption ($r_a = 2\gamma P_0$): $G = G_0(P_X/4 - P_0)$. Here $P_0 = p_0$, $P_X = \Sigma^{\infty}_{i=1} p_i$ and $P_0 + P_X = 1$. The corresponding 'truncated' CQD average occupancy is $\langle N^* \rangle = P_X$. Based on these expressions, $G = G_0(5P_X/4 - 1) = G_0(5\langle N^* \rangle/4 - 1)$, which yields $\langle N^*_{gain} \rangle = 0.8$ for the gain threshold. As expected, $\langle N^*_{gain} \rangle$ is lower than for the biexcitonic mechanism, for which $\langle N^*_{gain} \rangle \approx 1$. Even more important is that this scheme allows for achieving the lasing regime while maintaining the CQD medium in the single-exciton state. This leads to longer optical-gain lifetimes[91], which can, in principle, simplify the realization of optically pumped cw lasing, as well as lasing with d.c. electrical pumping. However, due to the fairly low saturated single-exciton gain ($\leq 0.25G_0$), the practical implementation of such a lasing regime would require a good resonator with low optical losses.

Emerging colloidal nanomaterials for lasing

Shape-controlled nanocrystals. Following the development of highly monodisperse CdSe CQDs[17], advances in colloidal synthesis enabled nanocrystals in which quantum confinement is weakened or completely eliminated in one (1D nanorods[27]) or two (2D NPLs[37,126]) dimensions, as well as heterostructures with mixed dimensionality, such as dot-in-rod nanocrystals[127,128] and tetrapods[127,128]. Demonstrations of lasing using shape-controlled structures followed shortly thereafter, facilitated by insights gained from prior studies of CdSe CQDs, including the critical role of dense films, short-pulse excitation and Auger recombination[61]. The first demonstration of lasing with anisotropic structures utilized CdSe nanorods[110], and was followed by observations of ASE and lasing for CdSe/CdS dot-in-rod nanocrystals[129–132] and tetrapods[133], and then CdSe NPLs and 2D heterostructures[75–77,102].

The simplest advantage conferred by shape control is that nanorods and NPLs exhibit large absorption cross-sections by virtue of their large physical dimensions. For example, in the case of CdSe nanorods, absorption cross-sections increase linearly with volume and reach ~10^{-13} cm^2 at 3.5 eV with no apparent saturation[134]. Absorption cross-sections of NPLs also exhibit *V*-scaling, and the reported values reach ~10^{-12} cm^2 at 3.1 eV for samples with lateral dimensions greater than 50 nm (REF.[135]). Anisotropic heterostructures show very high values of σ_a, too. In particular, for CdSe/CdS dot-in-rod nanocrystals[127], σ_a can be as high as ~10^{-13} cm^2, which is comparable to thick-shell core–shell CdSe/CdS g-CQDs[70]. Although these larger cross-sections are chiefly due to the increased number of unit cells in the structure, there is also an appreciable contribution due to improved optical field penetration dictated by the 1D and 2D morphologies[136,137]. In particular, local field factors can approach unity (no field attenuation) if light polarization is co-aligned with a longer dimension (normally, the direction of the transition dipole moment) of high-aspect-ratio nanorods and NPLs[136].

ASE thresholds of anisotropic nanostructures largely abide by a volume scaling relationship, similarly to CQDs (FIG. 2c). However, 2D NPLs often show lower thresholds (down to 0.8 μJ cm^{-2})[81] than CQDs of comparable volume (point 28 in FIG. 2c), which is likely a combined result of the enhanced local field factor and very large optical-gain coefficients achievable with 2D nanomaterials (as discussed later in this section). Importantly, NPL synthesis can achieve single-monolayer thickness control, which results in narrow ensemble emission linewidths comparable to those of individual NPLs[37,38,126,138]. This high level of monodispersity helps to further enhance optical gain and reduces reabsorption by decreasing spectral overlap between band-edge emission and absorption features[139].

Yet another benefit of a large nanostructure volume is slowing of Auger recombination, as illustrated in FIG. 3b for NPLs (orange symbols). In 1D or 2D nanocrystals, the restoration of translational momentum conservation, which does not hold in CQDs[140], may, in principle, result in an additional reduction of Auger recombination rates. This effect can contribute to the observed increase of biexciton Auger lifetimes in nanorods[141] and NPLs[102], although the measured trends are coarsely consistent with standard *V*-scaling (FIG. 3b).

There are other shape-specific features of Auger recombination in anisotropic nanostructures that might benefit lasing. In particular, for CdSe nanorods with large aspect ratios (~6 and higher), the scaling of higher-order Auger recombination rates with the number of e–h pairs changes from cubic to quadratic, because, in elongated nanostructures, e–h pairs behave as Coulombically bound 1D excitons[141]. This favours light amplification due to higher-order multiexcitons, which can be used to enable optical gain arising from higher-energy, above-band-gap transitions[72].

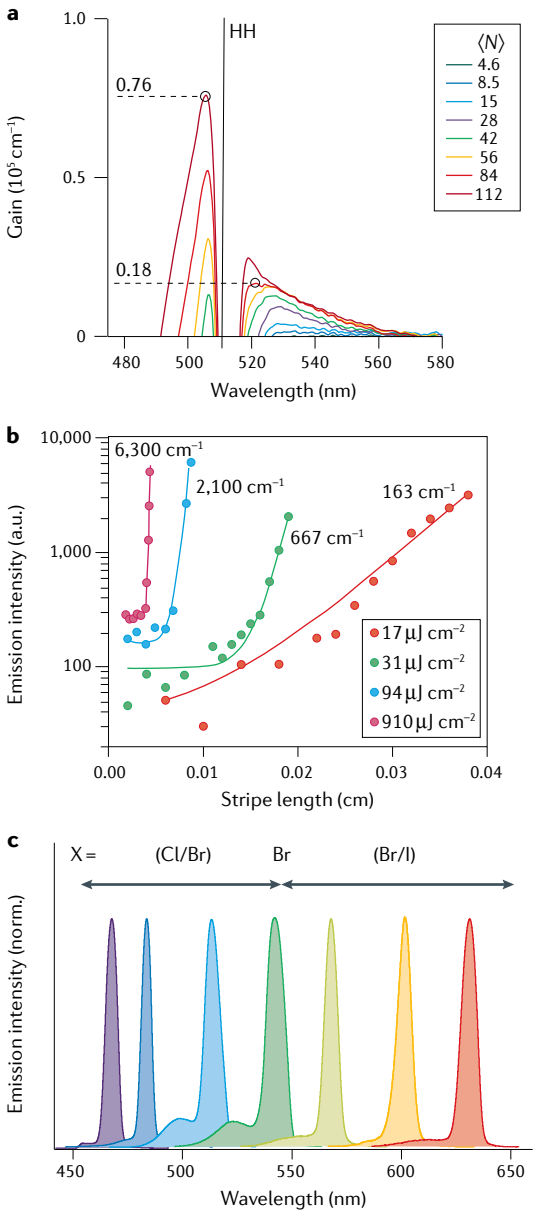

Fig. 6 | **Emerging colloidal lasing media. a** | Room-temperature optical-gain spectra of a stirred 4-monolayer CdSe nanoplatelet solution[149] for different average per-particle excitonic occupancies, ⟨*N*⟩. These spectra were collected 2.5 ps after excitation with 400-nm, 100-fs pulses. At smaller ⟨*N*⟩, optical gain occurs to the red of the heavy-hole (HH) excitonic peak at 512 nm; this gain was assigned to biexcitons. For ⟨*N*⟩ of 42 and higher, an additional gain band emerges at higher energies than the excitonic peak; this feature was assigned to unbound charge carriers (2D electron–hole plasma). **b** | Room-temperature modal gain measurements of a 4-monolayer CdSe nanoplatelet film using a variable-stripe-length method for per-pulse pump fluences ranging between 17 and 910 μJ cm^{-2} (150-fs, 400-nm pulsed excitation)[156]. **c** | Spectrally tunable amplified spontaneous emission in a family of $CsPbX_3$ perovskite colloidal quantum dots (X = Cl, Br, I) achieved by varying the composition of the halide component[84]. These measurements were performed using a 100-fs, 400-nm excitation. All perovskite colloidal quantum dots were cubes with a mean edge length of ~10 nm. Panel **a** is reproduced with permission from REF.[149], ACS. Panel **b** is reproduced with permission from REF.[156], ACS. Panel **c** is reproduced with permission from REF.[84], Springer Nature Limited.

The use of anisotropic heterostructures allows one to additionally impede Auger recombination through spatial separation of electrons and holes[142,143]. For example, in dot-in-rod CdSe/CdS heterostructures, the holes are confined to the CdSe core, whereas electrons tend to delocalize across the entire structure, especially for small core sizes. As a result of the spatial mismatch between electron and hole wavefunctions, the biexciton Auger lifetime becomes 6–10 times longer than for core-only particles[143]. Similar results have been obtained for type II core–crown CdSe/$CdSe_{1-x}Te_x$ hetero-NPLs, in which biexcitonic Auger decay slows by a factor of two versus core-only CQDs[144].

Optical amplification in shape-controlled colloidal nanostructures exhibits many similarities to optical amplification in CQDs. As in CdSe CQDs, ASE in CdSe nanorods and dot-in-rod particles occurs via biexcitonic gain, with a saturation consistent with a twofold degeneracy of the band-edge levels[72,145]. For NPLs, however, the gain mechanism still remains a subject of active investigation. In smaller-area structures, lasing likely occurs due to stimulated emission from biexcitonic states, like in CQDs[146,147]. In particular, the biexcitonic origin of the optical gain is consistent with reported ASE thresholds, which correspond to slightly more than one exciton per NPL, on average[76,77,102]. Interestingly, higher ASE and gain thresholds were observed for larger-area NPLs, suggesting that they are linked to the excitonic sheet density, rather than the total per-particle excitonic occupancy[147,148].

Gain mechanisms associated with Coulombically bound excitons and biexcitons ('excitonic molecules') were also invoked to explain peculiarities of light amplification in NPLs[77,147]. Due to the reduced dielectric screening typical of 2D structures[38], the effects of Coulombically bound species can be pronounced even at room temperature. In particular, the X–X attraction in NPLs can reach values of 30–45 meV, suggesting that excitons are able to form stable Coulombic biexcitons even at room temperature, as k_BT (~25 meV) in this case is still smaller than Δ_{XX} (REFS[77,147]). As a result, the photoexcited system can represent a mixture of thermally equilibrated excitons and biexcitons, both of which can contribute to optical gain[149] (FIG. 6a). Previous studies of epitaxial quantum wells showed that they could also exhibit biexcitonic optical gain and lasing at low temperatures when k_BT was lower than Δ_{XX} (REFS[150–152]).

At high excitation densities (⟨*N*⟩ > 50), lattice heating from Auger decay[153,154] and increased charge-carrier screening may lead to dissociation of Coulombically bound species, which is expected to enact a new optical-gain mechanism due to stimulated emission from a degenerate e–h plasma. This process was invoked to explain the emergence of a blue-shifted gain band in NPLs at high excitation intensities[149] (FIG. 6a). This e–h plasma gain is similar to the regime realized in epitaxial quantum wells at high temperatures, when k_BT becomes greater than Δ_{XX} (REFS[150,151]).

Due to their bosonic nature, many Coulombically bound e–h pairs can be accommodated in the same NPL, which impacts the maximal achievable gain[155]. For example, in CdSe CQDs and short nanorods, the band-edge states can accommodate no more than two excitons and, hence, gain saturation occurs at pump fluences that are roughly twice the gain threshold[90,141]. By contrast, the onset of gain saturation in CdSe NPLs depends on their area, and, in larger-size structures, it occurs at pump powers that are more than 10 times higher than the gain threshold[76,156]. As a result, optical gain can reach very large values of up to 6,300 cm^{-1} (REF.[156]) (FIG. 6b), inferred from the exponential growth of the edge-emission intensity measured as a function of the length of the excitation region shaped as a narrow stripe (so-called variable-stripe-length gain measurements).

Perovskite nanocrystals. Nanostructures based on Pb-halide perovskites such as $CsPbX_3$ (X = I, Br, Cl) represent a relatively recent addition to colloidal optical-gain media[34,84]. An attractive feature of these materials is that, in addition to traditional size control, their band gap can be manipulated via relatively straightforward anion-exchange reactions that allow one to readily tune the composition of the halide component[34,84,157,158] (FIG. 6c).

Some of the size-dependent trends reported for p-CQDs are similar to those of well-studied CdSe CQDs. At the same time, the absolute values of optical-gain-relevant characteristics, such as absorption cross-sections and Auger lifetimes, can differ considerably for similarly sized particles. In particular, as in the case of CdSe CQDs[68], the absorption cross-sections of $CsPbX_3$ p-CQDs measured at above-band-edge energies scale linearly with particle volume[106,107]. However, in order to match the magnitude of σ_a of CdSe CQDs, p-CQDs must be considerably larger. For example, side-by-side measurements of $CsPbBr_3$ and CdSe CQDs with respective per-particle volumes of 250 and 47.7 nm^3 indicated nearly identical absorption cross-sections of 3.5×10^{-15} cm^{-2} at 3.1 eV. This suggests that the absorption cross-section per unit semiconductor volume, or 'material absorption coefficient' ($\alpha_m = \sigma_a/V$), is lower for p-CQDs than for CdSe CQDs.

A similar situation is realized for Auger recombination time constants. As for more traditional CQD compositions, the biexciton Auger lifetimes of p-CQDs scale almost linearly with nanocrystal volume (FIG. 3b, open blue symbols). However, the absolute values of $\tau_{A,XX}$ are considerably shorter than for CdSe CQDs[106,107,159] (FIG. 3b, dark green symbols). As a result, the pre-factor χ (~0.06 ps nm^{-3}) is more than an order of magnitude smaller than in the standard V-scaling. Furthermore, unlike in other types of CQDs, for which χ has a 'universal' value of ~1 ps nm^{-3} independent of composition, in the case of p-CQDs, χ depends on both cation and anion compositions. In particular, for $CsPbX_3$ p-CQDs, $\tau_{A,XX}$ becomes shorter as the anion is switched from I to Br and, then, to Cl, while the dot size remains approximately the same[106,107,160]. The replacement of an A-site cation also affects Auger lifetimes. In particular, when Cs was switched to formamidinium or methylammonium, $\tau_{A,XX}$ increased by a factor of ~5, which was ascribed to increased Coulombic screening[161].

In addition to absorption cross-sections and Auger lifetimes, optical-gain properties of CQDs are strongly affected by degeneracies of band-edge states. Based on combined transient PL and transient absorption studies[106], in $CsPbX_3$ CQDs, both electron and hole states are twofold degenerate. This implies that, in the case of neutral dots, optical gain is due to biexcitons and the gain threshold is defined by a standard condition $\langle N_{gain} \rangle \approx 1$, as for CdSe-based CQDs. However, if evaluated in terms of the pump fluence (pulsed excitation), because of their lower material absorption coefficient, p-CQDs are expected to have higher optical-gain thresholds compared with CdSe nanostructures of a similar volume. Further, due to shorter Auger lifetimes, the disparity between the thresholds for perovskite and CdSe CQDs should be even greater in the case of cw pumping.

Experimental measurements of p-CQDs are consistent with the biexcitonic gain mechanism[162,163]. However, despite expectations for higher optical-gain thresholds, some of the reported ASE and lasing thresholds are actually lower than those for CdSe CQDs of similar size[82,84,164] (red squares in FIG. 2c). The reasons for this disparity have not been discussed in great detail in the literature. One possibility is uncontrolled photocharging of the p-CQDs, which can, in principle, lower the gain threshold due to charged-exciton effects. In fact, intentionally charged p-CQDs did show a reduction in the ASE threshold compared with neutral dots[82] (FIG. 2c, open red squares connected by an arrow).

Towards electrically pumped CQD lasers

Optical gain in the regime of electrical pumping. An important objective in the area of CQD-based optical-gain media is the demonstration of lasing with electrical excitation. The research into electrically pumped CQD lasers, or CQD laser diodes (abbreviated here as QLDs), represents a part of a broader effort targeting the realization of electrically excited lasing with solution-processable materials. This goal has been pursued across multiple fields, including semiconducting polymers[10,165–168], small molecules[169–173], carbon nanotubes[174–176] and perovskites[177–180].

As with other solution-processable gain media, one challenge in the case of CQDs is achieving population inversion with electrical charge injection. To quantify the current densities required to attain this regime, we introduce an 'electrical cross-section' σ_e. We use this quantity to relate the steady-state excitation rate to the current density (j) by $g = \sigma_e(j/e)$, where e is the elementary charge. CQDs are usually incorporated into an LED as a single monolayer (ML) sandwiched between electron and hole transport layers (ETL and HTL, respectively)[181,182]. The injected current flows preferentially through CQD semiconductor cores, which serve as current-focusing apertures (FIG. 7a, bottom). Due to the presence of surface-bound and unbound ligands, the areal filling factor (f) in a spin-coated CQD film is typically 0.5–0.6 (REF.[49]), versus ~0.9 for hexagonal close packing. As a result, the electrical cross-section is increased compared

with the CQD geometrical cross-section ($\sigma_g = \pi R^2$) by a factor of $1/f$ (FIG. 7a, top). In a typical CQD-LED, σ_e is ~$2\sigma_g$.

Based on the above considerations and our previous analysis of the case of cw optical excitation, the gain-threshold condition for electrically pumped devices is $j_{gain} = e/[\sigma_e(\tau_{XX}\tau_X)^{1/2}]$. As for cw optical pumping, the threshold current density increases as $(\tau_{XX})^{-1/2}$ with decreasing biexciton Auger lifetime. The detrimental role of Auger decay becomes even more apparent in the case of steady-state lasing, which is considerably more difficult to realize than the gain threshold. Based on the modelling of optically excited lasing[90], the cw excitation rate required to achieve half-saturated gain ($g = g_{½}$, $G = 0.5G_0$) can be computed from $g_{½} = (0.5/\tau_{XX})[1 + (1 + 12\tau_{XX}/\tau_X)^{1/2}]$. In the case of fast Auger decay ($\tau_{XX} \approx \tau_{A,XX}$ and $\tau_{XX} \ll \tau_X$), this expression leads to $g_{½} \approx 1/\tau_{A,XX}$. The corresponding current density is $j_{½} = e/(\sigma_e\tau_{A,XX})$, indicating that $j_{½}$ scales faster with Auger lifetime ($\propto 1/\tau_{A,XX}$) compared with the $(\tau_{A,XX})^{-1/2}$ scaling of j_{gain}. As a result, achieving lasing action becomes progressively more difficult with dots of smaller size due to the increasing Auger decay rate.

For example, for standard green-emitting CdSe CQDs with $R \approx 1.5$ nm, $\tau_{A,XX}$ is ~15 ps and τ_X is ~20 ns. Using these parameters and assuming $f = 0.5$, we obtain $j_{½} = 76$ kA cm^{-2}. This value is several orders of magnitude higher than maximal current densities achievable in CQD-LEDs (usually, <1 A cm^{-2}), which reemphasizes the need for effective approaches to control Auger recombination. Fortunately, such approaches are available to the CQD community. In particular, by exploiting compositional grading of the CQD interior, τ_{XX} can be extended to 1.5 ns (REF.[43]). Using this value, along with $\sigma_g = 2.8 \times 10^{-12}$ cm^2 (computed for CQDs from REF.[43]), we have obtained a $j_{½}$ of ~24 A cm^{-2}. Although this current density is higher than for standard CQD-LEDs, it is accessible with special high-j LED architectures, as discussed next.

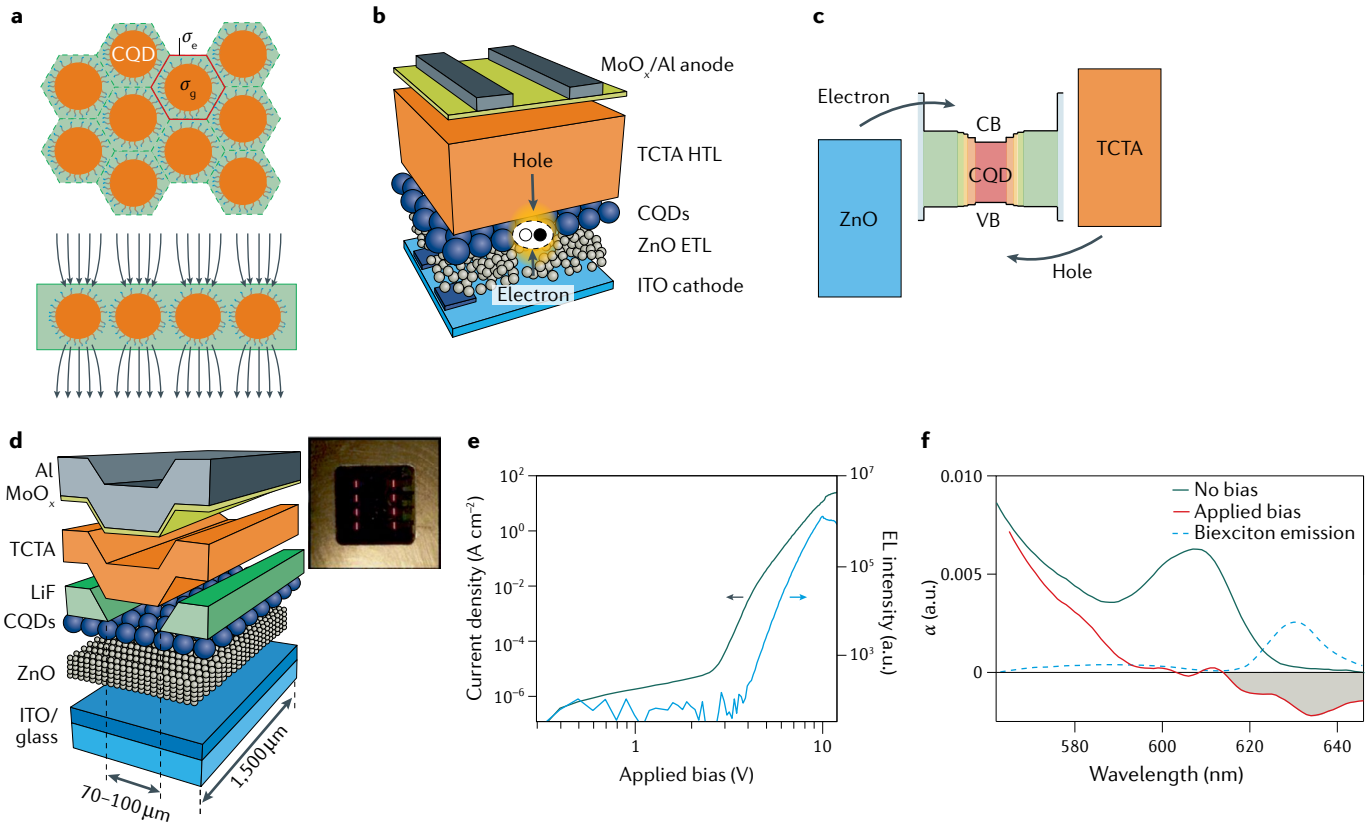

Fig. 7 | **Principles of operation of a colloidal quantum dot light-emitting diode and an example of a current-focusing optical-gain device. a** | In a colloidal quantum dot (CQD) film, semiconductor cores are surrounded by insulating organic molecules (top), which leads to a current-focusing effect (bottom). As a result, the CQD electrical cross-section (σ_e) becomes greater than its geometrical cross-section (σ_g). **b** | A schematic depiction of an inverted light-emitting diode[194], which comprises a single CQD monolayer sandwiched between an n-type electron transport layer (ETL) made of ZnO nanoparticles and a p-type tris(4-carbazoyl-9-ylphenyl)amine (TCTA)-based hole transport layer (HTL). The top (anode) and bottom (cathode) electrodes are made of MoO$_x$/Al and indium tin oxide (ITO), respectively. **c** | A simplified band diagram of the device shown in panel **b**, which illustrates that injection of electrons and holes into a CQD is facilitated by good matching between the charge transport layer's work functions and the energies of the CQD conduction band (CB) and valence band (VB) states. **d** | A high-current-density (j) inverted light-emitting diode architecture that comprises a dielectric LiF interlayer with a narrow slit limiting the injection area to a stripe of less than 100 μm in width. The inset shows a photograph of an 8-pixel device that employed this architecture[49]. **e** | An example of the dependence of current density (left axis) and electroluminescent (EL) intensity (right axis) on the applied bias for the current-focusing device in panel **d**, which allowed achievement of $j = 18$ A cm^{-2}. **f** | Optical absorption (α) measurements of the same device without (green line) and with (red line) applied bias ($j = 8$ A cm^{-2})[49]. The biased device exhibits optical gain ($\alpha < 0$), shown by grey shading. Its spectral position overlaps with the spectrum of a biexciton emission, shown by the blue dashed line. Panel **b** is adapted with permission from REF.[194], ACS. Panels **c**–**f** are adapted with permission from REF.[49], Springer Nature Limited.

High-current-density CQD-LEDs. In epitaxial QD laser diodes, a QD emitting layer is sandwiched between highly conductive n-type and p-type semiconductors and the injection area is limited in one or two dimensions to sub-100-μm sizes to achieve a current-focusing effect[183–185]. This architecture can support extremely high current densities of >1 kA cm^{-2} that are sufficient for realizing the lasing regime (which usually requires 100–1,000 A cm^{-2})[64,183,185,186]. In sharp contrast, in CQD-based devices, the achievement of current densities in excess of 1–2 A cm^{-2} already represents a serious challenge. Realization of this high-*j* regime is complicated by high resistivity of both the CQD film and charge transport layers (CTLs), their poor thermal conductivity and limited stability of CQDs at high temperatures that result from combined effects of ohmic[187–189] and Auger[154,190] heating.

The primary reason for high resistivity of CQD solids is the presence of organic ligands that create a thick insulating barrier at CQD surfaces. In CQD-LEDs, this problem has been tackled by reducing the thickness of the emitting layer to a single CQD ML placed directly between the CTLs (FIG. 7b). This design eliminates the need for dot-to-dot charge hopping and allows for efficient injection of both carriers if the CTL work functions are appropriately matched to the CB and VB energies of the CQDs. In the case of CdSe-based CQDs, such energy-matching can be achieved using an n-type ETL made of colloidal ZnO particles deposited on top of an indium tin oxide (ITO) electrode and a p-type HTL fabricated from organic molecules such as 4,4′-bis(N-carbazolyl)-1,1′-biphenyl (CBP) or tris(4-carbazoyl-9-ylphenyl)amine) (TCTA[49,191–194], FIG. 7c). This LED design, known as an 'inverted architecture', has allowed for demonstrating nearly ideal external quantum efficiencies approaching ~20%, which is the limit defined by a light extraction coefficient from a high-index semiconductor medium[195–198].

A necessary feature of high-performance CQD-LEDs is also good balance between electron and hole injection currents, which is required for avoiding unwanted charge accumulation and associated carrier losses due to nonradiative Auger decay. This process is often pointed to as being responsible for the external quantum efficiency roll-off or 'droop' observed at high current densities[192,194,199]. Because Auger recombination is accompanied by the release of a considerable amount of energy (~E_g per dot, per recombination event)[154,190,200], it also contributes to device heating, which, together with ohmic heating, accelerates LED degradation.

Imbalanced charge injection is expected to be a serious problem in optical-gain devices, as they necessarily operate at high current densities. In a standard CQD-LED, electron injection usually outpaces hole injection because the carrier mobility of an organic HTL (10^{-5}–10^{-3} cm^2 V^{-1} s^{-1}) is lower than that of a ZnO ETL (~10^{-3} cm^2 V^{-1} s^{-1})[191,201]. To tackle this problem at the device level, thin insulating barriers have been incorporated into an electron injection path[202,203], or ETL conductivity was intentionally reduced using poorly conductive additives[194,204]. In another approach, a wide-gap 'barrier' shell was added directly to a CQD in order to selectively impede electron injection without obstructing injection of holes[193,194,199,205]. A combination of device-level and CQD-level controls has enabled the demonstration of LEDs with ultra-high brightness[194] (~300,000 cd m^{-2}) operating virtually droop-free up to ~0.5 A cm^{-2}.

An important recent result of direct relevance to QLD development was the demonstration of CQD optical gain with d.c. electrical pumping[49]. This work employed engineered CdSe/Cd$_x$Zn$_{1-x}$Se/ZnSe$_{0.5}$S$_{0.5}$ cg-CQDs optimized for both strong suppression of Auger decay and balanced charge injection. They were incorporated into an inverted LED architecture containing an insulating LiF spacer with a narrow (<100-μm width) slit for current focusing (FIG. 7d). In addition to boosting the current density, this design, applied previously in high-*j* OLEDs[206–209], allowed for improved heat dissipation[210]. Furthermore, the use of dots with strongly suppressed Auger recombination, and, thereby, suppressed Auger heating, also helped mitigate problems due to thermal damage.

Using the above strategies, current densities of up to ~18 A cm^{-2} were achieved[49] (FIG. 7e), unprecedented for CQD-LEDs. This value was well above the gain threshold of ~7 A cm^{-2} computed from $j_{gain} = e/[\sigma_e(\tau_{XX}\tau_X)^{1/2}]$. The fabricated devices indeed showed unambiguous signatures of optical gain, which developed at 3–4 A cm^{-2} (FIG. 7f). The fact that the measured threshold was slightly lower than the estimated value could be due to nonuniformities in the film thickness (nominally ~1.5 ML) that would promote current flows through thinner film regions and, thereby, enhance the current-focusing effect.

Incorporation of an optical cavity. In addition to sufficiently high current densities, the achievement of electrically pumped CQD lasing requires device architectures that can simultaneously support electroluminescent (EL) and lasing functions. To realize such a dual-function device, one needs to incorporate an optical resonator into an LED in such a way as to not obstruct charge injection pathways and, at the same time, avoid quenching of the lasing modes by conductive CTLs.

Previous research into optically pumped CQD lasing has explored various cavity designs, including Fabry–Pérot[93], spherical[211] and microring resonators[212], vertical cavities[75] and DFB gratings[113]. Among those, a DFB resonator adjacent to a CQD active region satisfies all requirements of a laser-diode architecture. In particular, it can be readily incorporated into an LED stack by simply patterning one of the existing device layers. Further, the cavity resonances can be easily adjusted by varying the grating period in the lateral device plane, without disturbing the device vertical structure, which can, thus, be used to independently tune carrier injection.

Previous works on organic materials and perovskites demonstrated the possibility of obtaining optically pumped lasing using a DFB resonator integrated into functional LEDs[213,214] and light-emitting field-effect transistors[215]. A DFB cavity was also combined with a high-*j* current-focusing EL structure that utilized blue-emitting small organic molecules[173]. When excited with short, 400-ns electrical pulses, these devices were

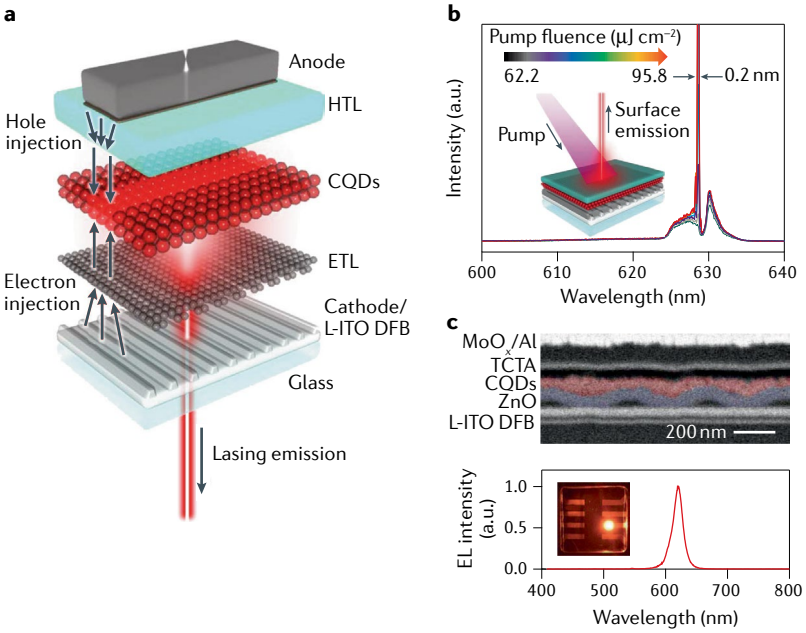

Fig. 8 | **A dual-function colloidal quantum dot light-emitting diode with an integrated distributed feedback cavity. a** | A colloidal quantum dot laser diode (QLD) design proposed in REF.[50]. It utilizes a current-focusing inverted light-emitting diode architecture that contains a second-order distributed feedback (DFB) cavity integrated into a bottom low-index indium tin oxide (L-ITO) electrode. The L-ITO is used to reduce optical mode leakage out of the colloidal quantum dot (CQD) layer. **b** | A fabricated prototype device with a QLD-like structure exhibits strong lasing performance under optical excitation with 130-fs, 400-nm pulses (pump fluences are indicated in the legend). The active region thickness is only three CQD monolayers. **c** | A cross-sectional scanning electron microscopy image of the device schematically depicted in panel **b** after it is completed with a top MoO_x/Al electrode (top). This device exhibits bright electroluminescence (EL) under electrical bias (inset), with a spectrum peak at 621 nm (bottom)[50]. ETL, electron transport layer; HTL, hole transport layer; TCTA, tris(4-carbazoyl-9-ylphenyl) amine. The figure is adapted with permission from REF.[50], Springer Nature Limited.

capable of generating extremely high current densities (up to 5.7 kA cm^{-2} before breakdown), sufficient to observe coherent laser light mixed with incoherent EL.

Recently, dual-function LED/optically pumped laser structures were also demonstrated for CQDs[50]. These devices, which had a QLD-like architecture (FIG. 8a), contained a second-order DFB cavity integrated into a bottom electron-injecting electrode made of low-index ITO (L-ITO). A p-i-n device stack comprising a ZnO ETL, a CQD active layer and a TCTA HTL was assembled on top of the patterned electrode. Due to a carefully engineered refractive-index profile across the device stack, the modal gain was sufficiently high to support optically excited lasing, even with an ultra-thin (~50 nm) optical-gain medium containing only three CQD MLs (FIG. 8b). Importantly, these devices also showed good EL performance as standard LEDs (FIG. 8c). However, the maximum current density was not sufficient for realizing an optical-gain regime. The primary limitation was a high resistivity of the bottom electrode (made of ITO diluted with SiO_2), because of which the device breakdown occurred at fairly low current densities of ~0.2 A cm^{-2}. In principle, this problem can be tackled through the optimization of a mode cross-section profile in the presence of the 'undiluted-ITO' electrode. The use of current focusing and, if necessary, short-electrical-pulse excitation can also help boost the current densities achievable in the pre-breakdown regime.

Summary and outlook

It has already been 20 years since proof-of-principle experiments that demonstrated the feasibility of light amplification in CQD materials and established the principles of CQD lasing[61]. Colloidal nanostructures are no longer just the subject of scientific curiosity, as back then, but are industrial-grade optical and optoelectronic materials that are already applied in modern televisions and displays, as well as other commercialization-ready devices, such as colour-adjustable light bulbs and luminescent sunlight collectors. Despite tremendous advances in the CQD field in general, CQD lasers are still to be found only in a research lab setting. In similarity to 20 years ago, the primary challenge remains the same: fast deactivation of a CQD gain medium due to intrinsic Auger recombination.

The situation, however, is about to change. Over the past few years, several approaches have been developed to tackle the problem of Auger decay. Some of them attack this challenge at the gain-mechanism level and others aim at direct control of Auger recombination rates. Two demonstrated nonbiexcitonic mechanisms are single-exciton gain, implemented with type II CQDs[91], and charged-exciton gain, achieved using electrochemical[216] or photochemical CQD doping[43,44]. The idea behind both is to effectively reduce the degeneracy of band-edge states so that biexcitons are no longer required to produce optical gain.

A single-exciton mechanism employs X–X repulsion to spectrally decouple the emitting and absorbing transitions originating from the single-exciton state, which turns excitons from gain-neutral to gain-active species. However, the very strong X–X repulsion required to enact this mechanism is not readily available in nanostructures commonly used in lasing experiments, such as CdSe/CdS g-CQDs or CdSe-based NPLs. This indicates the need for further synthetic developments in the area of lasing-grade type II nanostructures that could enable strong X–X interactions and, at the same time, exhibit high monodispersity (that is, narrow linewidth), excellent light-emission properties and high photostability. The availability of such structures would facilitate the development of low-threshold cw lasers, which could be operated using incoherent pump sources, such as standard LEDs. This would also relax the constraints due to minimal CQD density in a gain medium and potentially allow for achieving lasing with low-density CQD materials, such as CQD solutions and polymer composites.

In the charged/doped-CQD scheme, the band-edge degeneracy is reduced by blocking the band-edge states with uncompensated carriers. In this approach, optical gain is due to charged excitons. Although this does not completely eliminate Auger recombination, it weakens its influence, as Auger lifetimes of both singly and doubly charged excitons are slower than that of a biexciton. The charge-exciton scheme is especially effective if applied

together with Auger decay engineering. In particular, the combination of these approaches allowed for demonstrating well-behaved DFB lasers with ultra-low thresholds of only ~0.3 excitons per dot on average or ~2 μJ cm^{-2} (REF.[43]).

Recent experimental studies have provided several successful demonstrations of direct control of Auger decay using CQDs with a compositionally graded interior[47,49]. Lately, it was implemented with continuously graded CdSe/Cd$_x$Zn$_{1-x}$Se/ZnSe$_{0.5}$S$_{0.5}$ cg-CQDs, which allowed for boosting the biexciton PL QYs to ~45%. Importantly, strong suppression of Auger decay was realized while still preserving strong quantum confinement, with ΔE_{conf} of ~10k_BT at room temperature.

The progress in Auger decay engineering was essential to recent advances of direct relevance to the development of electrically pumped CQD lasers. In particular, effective control of Auger decay and associated suppression of Auger heating were key to the first demonstration of electrically excited optical gain with cg-CQDs incorporated into current-focusing LEDs[49]. These dots were also an essential part of the recent successful demonstration of dual-function EL/lasing devices[50], which showed strong lasing performance employing only three CQD MLs as a gain medium.

The focus of this Review has been on CdSe-based nanostructures, which represent the most synthetically advanced colloidal nanomaterials. These nanocrystals are well suited for applications in the range of visible wavelengths. However, due to a fairly large bulk CdSe band gap (1.75 eV), they cannot be applied in the infrared (IR). The best developed IR-active colloidal nanomaterials are PbS and PbSe nanocrystals[217], which have been extensively studied in the context of prospective photovoltaic applications[218,219]. With proper surface treatment and/or shelling procedures, PbSe(S) CQDs can also exhibit high PL QYs[220–222]. However, because of the eightfold degeneracy of their band-edge states, they exhibit a very high optical-gain threshold of 4 excitons per dot[223]. This greatly complicates the realization of practical lasing devices, as Auger lifetimes scale very rapidly with exciton multiplicity[101].

To tackle this problem, a recent study[224] applied a charged-CQD gain scheme to PbS CQDs. In particular, using heavily doped CQDs, the authors of this work were able to reduce the gain threshold to $\langle N_{gain}\rangle \approx 1$. This interesting result proves the generality of the charged-exciton gain scheme and, in addition, demonstrates a practical approach for its implementation in the case of IR materials. Further developments in this area can take advantage of a large arsenal of previously developed synthetic tools that can, in particular, be applied to realize compositional grading for suppressing Auger recombination.

During the past two decades, CQD lasing has grown into a mature field that has come very close to a point where it can become a practical technology. An important milestone towards this goal would be the demonstration of electrically pumped CQD lasers. Just a few years ago, the realization of such devices was widely deemed impossible due to problems such as ultra-fast Auger decay, insufficient current densities in CQD LEDs, thermal damage issues and difficulties in combining EL and lasing functions in the same CQD device. The majority of these problems has been recently resolved. Now, we are just one short step away from a functional CQD laser diode.

Published online 15 February 2021

1. Xie, W. et al. On-chip integrated quantum-dot–silicon-nitride microdisk lasers. *Adv. Mater.* **29**, 1604866 (2017).
2. Cegielski, P. J. et al. Monolithically integrated perovskite semiconductor lasers on silicon photonic chips by scalable top-down fabrication. *Nano Lett.* **18**, 6915–6923 (2018).
3. Kim, J. T. et al. Graphene-based plasmonic waveguide devices for electronic-photonic integrated circuit. *Opt. Laser Technol.* **106**, 76–86 (2018).
4. Amemiya, T. et al. Organic membrane photonic integrated circuits (OMPICs). *Opt. Express* **25**, 18537–18552 (2017).
5. Jung, H. et al. Efficient on-chip integration of a colloidal quantum dot photonic crystal band-edge laser with a coplanar waveguide. *Opt. Express* **25**, 32919–32930 (2017).
6. Clark, J. & Lanzani, G. Organic photonics for communications. *Nat. Photonics* **4**, 438–446 (2010).
7. Grivas, C. & Pollnau, M. Organic solid-state integrated amplifiers and lasers. *Laser Photonics Rev.* **6**, 419–462 (2012).
8. Vannahme, C., Klinkhammer, S., Lemmer, U. & Mappes, T. Plastic lab-on-a-chip for fluorescence excitation with integrated organic semiconductor lasers. *Opt. Express* **19**, 8179–8186 (2011).
9. Vannahme, C. et al. Integration of organic semiconductor lasers and single-mode passive waveguides into a PMMA substrate. *Microelectron. Eng.* **87**, 693–695 (2010).
10. Karl, M. et al. Flexible and ultra-lightweight polymer membrane lasers. *Nat. Commun.* **9**, 1525 (2018).
11. Zhang, C. et al. Organic printed photonics: from microring lasers to integrated circuits. *Sci. Adv.* **1**, e1500257 (2015).
12. Kang, D., Chen, H. & Yoon, J. Stretchable, skin-conformal microscale surface-emitting lasers with dynamically tunable spectral and directional selectivity. *Appl. Phys. Lett.* **114**, 041103 (2019).
13. Vollmer, F. & Arnold, S. Whispering-gallery-mode biosensing: label-free detection down to single molecules. *Nat. Methods* **5**, 591–596 (2008).
14. Chandrasekar, R., Lapin, Z., Nichols, A., Braun, R. & Fountain, A. Photonic integrated circuits for Department of Defense-relevant chemical and biological sensing applications: state-of-the-art and future outlooks. *Opt. Eng.* **58**, 020901 (2019).
15. Retolaza, A. et al. Organic distributed feedback laser for label-free biosensing of ErbB2 protein biomarker. *Sens. Actuators B Chem.* **223**, 261–265 (2016).
16. Chen, Y.-C. & Fan, X. Biological lasers for biomedical applications. *Adv. Opt. Mater.* **7**, 1900377 (2019).
17. Murray, C. B., Norris, D. J. & Bawendi, M. G. Synthesis and characterization of nearly monodisperse CdE (E = sulfur, selenium, tellurium) semiconductor nanocrystallites. *J. Am. Chem. Soc.* **115**, 8706–8715 (1993).
18. Pietryga, J. M. et al. Spectroscopic and device aspects of nanocrystal quantum dots. *Chem. Rev.* **116**, 10513–10622 (2016).
19. Kim, J. Y., Voznyy, O., Zhitomirsky, D. & Sargent, E. H. 25th anniversary article: Colloidal quantum dot materials and devices: a quarter-century of advances. *Adv. Mater.* **25**, 4986–5010 (2013).
20. Kagan, C. R., Lifshitz, E., Sargent, E. H. & Talapin, D. V. Building devices from colloidal quantum dots. *Science* **353**, aac5523 (2016).
21. Kagan, C. R. Flexible colloidal nanocrystal electronics. *Chem. Soc. Rev.* **48**, 1626–1641 (2019).
22. Ekimov, A. I. & Onushchenko, A. A. Quantum size effect in three-dimensional microscopic semiconductor crystals. *JETP Lett.* **34**, 345–349 (1981).
23. Borrelli, N. F., Hall, D. W., Holland, H. J. & Smith, D. W. Quantum confinement effects of semiconducting microcrystallites in glass. *J. Appl. Phys.* **61**, 5399–5409 (1987).
24. Vandyshev, Y. V., Dneprovskiĭ, V. S. & Klimov, V. I. Manifestation of dimensional quantization levels in the nonlinear transmission spectra of semiconductor microcrystals. *JETP Lett.* **53**, 314–318 (1991).
25. Vandyshev, Y., Dneprovskii, V., Klimov, V. & Okorokov, D. Lasing on a transition between quantum-well levels in a quantum dot. *JETP Lett.* **54**, 442–445 (1991).
26. Bruchez, M., Moronne, M., Gin, P., Weiss, S. & Alivisatos, A. P. Semiconductor nanocrystals as fluorescent biological labels. *Science* **281**, 2013–2016 (1998).
27. Peng, X. et al. Shape control of CdSe nanocrystals. *Nature* **404**, 59–61 (2000).
28. Hines, M. A. & Guyot-Sionnest, P. Synthesis and characterization of strongly luminescing ZnS-capped CdSe nanocrystals. *J. Phys. Chem.* **100**, 468–471 (1996).
29. Kim, S., Fisher, B., Eisler, H.-J. & Bawendi, M. Type-II quantum dots: CdTe/CdSe(core/shell) and CdSe/ZnTe(core/shell) heterostructures. *J. Am. Chem. Soc.* **125**, 11466–11467 (2003).
30. Murray, C. B., Kagan, C. R. & Bawendi, M. G. Synthesis and characterization of monodisperse nanocrystals and close-packed nanocrystal assemblies. *Annu. Rev. Mater. Sci.* **30**, 545–610 (2000).
31. Qu, L., Peng, Z. A. & Peng, X. Alternative routes toward high quality CdSe nanocrystals. *Nano Lett.* **1**, 333–337 (2001).
32. Peng, X., Schlamp, M. C., Kadavanich, A. V. & Alivisatos, A. P. Epitaxial growth of highly luminescent CdSe/CdS core/shell nanocrystals with photostability and electronic accessibility. *J. Am. Chem. Soc.* **119**, 7019–7029 (1997).
33. Pietryga, J. M. et al. Pushing the band gap envelope: mid-infrared emitting colloidal PbSe quantum dots. *J. Am. Chem. Soc.* **126**, 11752–11753 (2004).
34. Protesescu, L. et al. Nanocrystals of cesium lead halide perovskites ($CsPbX_3$, X = Cl, Br, and I): Novel optoelectronic materials showing bright emission with wide color gamut. *Nano Lett.* **15**, 3692–3696 (2015).

35. Peng, Z. A. & Peng, X. Nearly monodisperse and shape-controlled CdSe nanocrystals via alternative routes: nucleation and growth. *J. Am. Chem. Soc.* **124**, 3343–3353 (2002).
36. Li, L.-s, Walda, J., Manna, L. & Alivisatos, A. P. Semiconductor nanorod liquid crystals. *Nano Lett.* **2**, 557–560 (2002).
37. Joo, J., Son, J. S., Kwon, S. G., Yu, J. H. & Hyeon, T. Low-temperature solution-phase synthesis of quantum well structured CdSe nanoribbons. *J. Am. Chem. Soc.* **128**, 5632–5633 (2006).
38. Ithurria, S. et al. Colloidal nanoplatelets with two-dimensional electronic structure. *Nat. Mater.* **10**, 936–941 (2011).
39. Ithurria, S. & Talapin, D. V. Colloidal atomic layer deposition (c-ALD) using self-limiting reactions at nanocrystal surface coupled to phase transfer between polar and nonpolar media. *J. Am. Chem. Soc.* **134**, 18585–18590 (2012).
40. Manna, L., Milliron, D. J., Meisel, A., Scher, E. C. & Alivisatos, A. P. Controlled growth of tetrapod-branched inorganic nanocrystals. *Nat. Mater.* **2**, 382–385 (2003).
41. Enright, M. J. et al. Seeded growth of nanoscale semiconductor tetrapods: generality and the role of cation exchange. *Chem. Mater.* **32**, 4774–4784 (2020).
42. Pang, Q. et al. CdSe nano-tetrapods: controllable synthesis, structure analysis, and electronic and optical properties. *Chem. Mater.* **17**, 5263–5267 (2005).
43. Kozlov, O. V. et al. Sub–single-exciton lasing using charged quantum dots coupled to a distributed feedback cavity. *Science* **365**, 672–675 (2019).
44. Wu, K., Park, Y.-S., Lim, J. & Klimov, V. I. Towards zero-threshold optical gain using charged semiconductor quantum dots. *Nat. Nanotechnol.* **12**, 1140–1147 (2017).
45. Cragg, G. E. & Efros, A. L. Suppression of Auger processes in confined structures. *Nano Lett.* **10**, 313–317 (2010).
46. Park, Y.-S., Bae, W. K., Padilha, L. A., Pietryga, J. M. & Klimov, V. I. Effect of the core/shell interface on Auger recombination evaluated by single-quantum-dot spectroscopy. *Nano Lett.* **14**, 396–402 (2014).
47. Bae, W. K. et al. Controlled alloying of the core–shell interface in CdSe/CdS quantum dots for suppression of Auger recombination. *ACS Nano* **7**, 3411–3419 (2013).
48. Fan, F. et al. Continuous-wave lasing in colloidal quantum dot solids enabled by facet-selective epitaxy. *Nature* **544**, 75–79 (2017).
49. Lim, J., Park, Y.-S. & Klimov, V. I. Optical gain in colloidal quantum dots achieved with direct-current electrical pumping. *Nat. Mater.* **17**, 42–48 (2018).
50. Roh, J., Park, Y.-S., Lim, J. & Klimov, V. I. Optically pumped colloidal-quantum-dot lasing in LED-like devices with an integrated optical cavity. *Nat. Commun.* **11**, 271 (2020).
51. Wang, Y. & Sun, H. Advances and prospects of lasers developed from colloidal semiconductor nanostructures. *Prog. Quantum Electron.* **60**, 1–29 (2018).
52. Geiregat, P., Van Thourhout, D. & Hens, Z. A bright future for colloidal quantum dot lasers. *NPG Asia Mater.* **11**, 41 (2019).
53. Kovalenko, M. V. et al. Prospects of nanoscience with nanocrystals. *ACS Nano* **9**, 1012–1057 (2015).
54. Erdem, T. & Demir, H. V. Colloidal nanocrystals for quality lighting and displays: milestones and recent developments. *Nanophotonics* **5**, 74–95 (2016).
55. Efros, A. L. et al. Band-edge exciton in quantum dots of semiconductors with a degenerate valence band: Dark and bright exciton states. *Phys. Rev. B* **54**, 4843–4856 (1996).
56. Efros, A. L. & Rosen, M. The electronic structure of semiconductor nanocrystals. *Annu. Rev. Mater. Sci.* **30**, 475–521 (2000).
57. Klimov, V. I. Mechanisms for photogeneration and recombination of multiexcitons in semiconductor nanocrystals: implications for lasing and solar energy conversion. *J. Phys. Chem. B* **110**, 16827–16845 (2006).
58. Arakawa, Y. & Sakaki, H. Multidimensional quantum well laser and temperature dependence of its threshold current. *Appl. Phys. Lett.* **40**, 939–941 (1982).
59. Asada, M., Miyamoto, Y. & Suematsu, Y. Gain and the threshold of three-dimensional quantum-box lasers. *IEEE J. Quantum Electron.* **22**, 1915–1921 (1986).
60. Bernard, M. G. A. & Duraffourg, G. Laser conditions in semiconductors. *Phys. Status Solidi B* **1**, 699–703 (1961).
61. Klimov, V. I. et al. Optical gain and stimulated emission in nanocrystal quantum dots. *Science* **290**, 314–317 (2000).
62. Ledentsov, N. N. et al. Optical properties of heterostructures with InGaAs-GaAs quantum clusters. *Semiconductors* **28**, 832–834 (1994).
63. Kirstaedter, N. et al. Low threshold, large T_0 injection laser emission from (InGa)As quantum dots. *Electron. Lett.* **30**, 1416–1417 (1994).
64. Grundmann, M. The present status of quantum dot lasers. *Phys. E* **5**, 167–184 (1999).
65. Kageyama, T. et al. in *2011 Conference on Lasers and Electro-Optics Europe and 12th European Quantum Electronics Conference (CLEO EUROPE/EQEC)* (IEEE, 2011).
66. Klimov, V. I., Mikhailovsky, A. A., McBranch, D. W., Leatherdale, C. A. & Bawendi, M. G. Quantization of multiparticle Auger rates in semiconductor quantum dots. *Science* **287**, 1011–1013 (2000).
67. Park, Y.-S., Lim, J. & Klimov, V. I. Asymmetrically strained quantum dots with non-fluctuating single-dot emission spectra and subthermal room-temperature linewidths. *Nat. Mater.* **18**, 249–255 (2019).
68. Klimov, V. I. Optical nonlinearities and ultrafast carrier dynamics in semiconductor nanocrystals. *J. Phys. Chem. B* **104**, 6112–6123 (2000).
69. Jasieniak, J., Smith, L., van Embden, J., Mulvaney, P. & Califano, M. Re-examination of the size-dependent absorption properties of CdSe quantum dots. *J. Phys. Chem. C* **113**, 19468–19474 (2009).
70. García-Santamaría, F. et al. Suppressed Auger recombination in "giant" nanocrystals boosts optical gain performance. *Nano Lett.* **9**, 3482–3488 (2009).
71. Bisschop, S., Geiregat, P., Aubert, T. & Hens, Z. The impact of core/shell sizes on the optical gain characteristics of CdSe/CdS quantum dots. *ACS Nano* **12**, 9011–9021 (2018).
72. Htoon, H., Hollingworth, J. A., Malko, A. V., Dickerson, R. & Klimov, V. I. Light amplification in semiconductor nanocrystals: quantum rods versus quantum dots. *Appl. Phys. Lett.* **82**, 4776–4778 (2003).
73. Moreels, I. et al. Nearly temperature-independent threshold for amplified spontaneous emission in colloidal CdSe/CdS quantum dot-in-rods. *Adv. Mater.* **24**, OP231–OP235 (2012).
74. Krahne, R., Zavelani-Rossi, M., Lupo, M. G., Manna, L. & Lanzani, G. Amplified spontaneous emission from core and shell transitions in CdSe/CdS nanorods fabricated by seeded growth. *Appl. Phys. Lett.* **98**, 063105 (2011).
75. Guzelturk, B., Kelestemur, Y., Olutas, M., Delikanli, S. & Demir, H. V. Amplified spontaneous smission and lasing in colloidal nanoplatelets. *ACS Nano* **8**, 6599–6605 (2014).
76. She, C. et al. Low-threshold stimulated emission using colloidal quantum wells. *Nano Lett.* **14**, 2772–2777 (2014).
77. Grim, J. Q. et al. Continuous-wave biexciton lasing at room temperature using solution-processed quantum wells. *Nat. Nanotechnol.* **9**, 891–895 (2014).
78. Chhantyal, P. et al. Low threshold room temperature amplified spontaneous emission in 0D, 1D and 2D quantum confined systems. *Sci. Rep.* **8**, 3962 (2018).
79. Guzelturk, B. et al. High-efficiency optical gain in type-II semiconductor nanocrystals of alloyed colloidal quantum wells. *J. Phys. Chem. Lett.* **8**, 5317–5324 (2017).
80. Altintas, Y. et al. Giant alloyed hot injection shells enable ultralow optical gain threshold in colloidal quantum wells. *ACS Nano* **13**, 10662–10670 (2019).
81. Taghipour, N. et al. Sub-single exciton optical gain threshold in colloidal semiconductor quantum wells with gradient alloy shelling. *Nat. Commun.* **11**, 3305 (2020).
82. Wang, Y., Zhi, M., Chang, Y.-Q., Zhang, J.-P. & Chan, Y. Stable, ultralow threshold amplified spontaneous emission from $CsPbBr_3$ nanoparticles exhibiting trion gain. *Nano Lett.* **18**, 4976–4984 (2018).
83. Tong, Y. et al. Highly luminescent cesium lead halide perovskite nanocrystals with tunable composition and thickness by ultrasonication. *Angew. Chem. Int. Ed.* **55**, 13887–13892 (2016).
84. Yakunin, S. et al. Low-threshold amplified spontaneous emission and lasing from colloidal nanocrystals of caesium lead halide perovskites. *Nat. Commun.* **6**, 8056 (2015).
85. Malko, A. V. et al. From amplified spontaneous emission to microring lasing using nanocrystal quantum dot solids. *Appl. Phys. Lett.* **81**, 1303–1305 (2002).
86. Wang, Y. et al. Unraveling the ultralow threshold stimulated emission from CdZnS/ZnS quantum dot and enabling high-Q microlasers. *Laser Photonics Rev.* **9**, 507–516 (2015).
87. Guzelturk, B., Kelestemur, Y., Akgul, M. Z., Sharma, V. K. & Demir, H. V. Ultralow threshold one-photon- and two-photon-pumped optical gain media of blue-emitting colloidal quantum dot films. *J. Phys. Chem. Lett.* **5**, 2214–2218 (2014).
88. Gao, S. et al. Lasing from colloidal InP/ZnS quantum dots. *Opt. Express* **19**, 5528–5535 (2011).
89. Di Stasio, F., Polovitsyn, A., Angeloni, I., Moreels, I. & Krahne, R. Broadband amplified spontaneous emission and random lasing from wurtzite CdSe/CdS "giant-shell" nanocrystals. *ACS Photonics* **3**, 2083–2088 (2016).
90. Park, Y.-S., Bae, W. K., Baker, T., Lim, J. & Klimov, V. I. Effect of Auger recombination on lasing in heterostructured quantum dots with engineered core/shell interfaces. *Nano Lett.* **15**, 7319–7328 (2015).
91. Klimov, V. I. et al. Single-exciton optical gain in semiconductor nanocrystals. *Nature* **447**, 441–446 (2007).
92. Wang, Y. et al. Stimulated emission and lasing from CdSe/CdS/ZnS core-multi-shell quantum dots by simultaneous three-photon absorption. *Adv. Mater.* **26**, 2954–2961 (2014).
93. Dang, C. et al. Red, green and blue lasing enabled by single-exciton gain in colloidal quantum dot films. *Nat. Nanotechnol.* **7**, 335–339 (2012).
94. Robel, I., Gresback, R., Kortshagen, U., Schaller, R. D. & Klimov, V. I. Universal size-dependent trend in Auger recombination in direct-gap and indirect-gap semiconductor nanocrystals. *Phys. Rev. Lett.* **102**, 177404 (2009).
95. Wang, L.-W., Califano, M., Zunger, A. & Franceschetti, A. Pseudopotential theory of Auger processes in CdSe quantum dots. *Phys. Rev. Lett.* **91**, 056404 (2003).
96. Efros, A. L. & Rosen, M. Random telegraph signal in the photoluminescence intensity of a single quantum dot. *Phys. Rev. Lett.* **78**, 1110–1113 (1997).
97. Kharchenko, V. A. & Rosen, M. Auger relaxation processes in semiconductor nanocrystals and quantum wells. *J. Lumin.* **70**, 158–169 (1996).
98. Dneprovskii, V. S. et al. Time-resolved luminescence of CdSe microcrystals. *Solid State Commun.* **74**, 555–557 (1990).
99. Roussignol, P. et al. Time-resolved direct observation of Auger recombination in semiconductor-doped glasses. *Appl. Phys. Lett.* **51**, 1882–1884 (1987).
100. Stewart, J. T. et al. Comparison of carrier multiplication yields in PbS and PbSe nanocrystals: the role of competing energy-loss processes. *Nano Lett.* **12**, 622–628 (2011).
101. Klimov, V. I., McGuire, J. A., Schaller, R. D. & Rupasov, V. I. Scaling of multiexciton lifetimes in semiconductor nanocrystals. *Phys. Rev. B* **77**, 195324 (2008).
102. She, C. et al. Red, yellow, green, and blue amplified spontaneous emission and lasing using colloidal CdSe nanoplatelets. *ACS Nano* **9**, 9475–9485 (2015).
103. Pandey, A. & Guyot-Sionnest, P. Multicarrier recombination in colloidal quantum dots. *J. Chem. Phys.* **127**, 111104 (2007).
104. Fisher, B., Caruge, J.-M., Chan, Y.-T., Halpert, J. & Bawendi, M. G. Multiexciton fluorescence from semiconductor nanocrystals. *Chem. Phys.* **318**, 71–81 (2005).
105. Achermann, M., Hollingsworth, J. A. & Klimov, V. I. Multiexcitons confined within a subexcitonic volume: spectroscopic and dynamical signatures of neutral and charged biexcitons in ultrasmall semiconductor nanocrystals. *Phys. Rev. B* **68**, 245302 (2003).
106. Makarov, N. S. et al. Spectral and dynamical properties of single excitons, biexcitons, and trions in cesium-lead-halide perovskite quantum dots. *Nano Lett.* **16**, 2349–2362 (2016).
107. Castañeda, J. A. et al. Efficient biexciton interaction in perovskite quantum dots under weak and strong confinement. *ACS Nano* **10**, 8603–8609 (2016).
108. McGuire, J. A., Joo, J., Pietryga, J. M., Schaller, R. D. & Klimov, V. I. New aspects of carrier multiplication in semiconductor nanocrystals. *Acc. Chem. Res.* **41**, 1810–1819 (2008).
109. Crooker, S. A., Hollingsworth, J. A., Tretiak, S. & Klimov, V. I. Spectrally resolved dynamics of energy transfer in quantum-dot assemblies: towards engineered energy flows in artificial materials. *Phys. Rev. Lett.* **89**, 186802 (2002).
110. Kazes, M., Lewis, D. Y., Ebenstein, Y., Mokari, T. & Banin, U. Lasing from semiconductor quantum rods in a cylindrical microcavity. *Adv. Mater.* **14**, 317–321 (2002).

111. Eisler, H.-J. et al. Color-selective semiconductor nanocrystal laser. *Appl. Phys. Lett.* **80**, 4614–4616 (2002).
112. Klimov, V. I. & Bawendi, M. G. Ultrafast carrier dynamics, optical amplification, and lasing in nanocrystal quantum dots. *MRS Bull.* **26**, 998–1004 (2001).
113. Adachi, M. M. et al. Microsecond-sustained lasing from colloidal quantum dot solids. *Nat. Commun.* **6**, 8694 (2015).
114. Park, Y.-S., Lim, J., Makarov, N. S. & Klimov, V. I. Effect of interfacial alloying versus "volume scaling" on Auger recombination in compositionally graded semiconductor quantum dots. *Nano Lett.* **17**, 5607–5613 (2017).
115. García-Santamaría, F. et al. Breakdown of volume scaling in Auger recombination in CdSe/CdS heteronanocrystals: the role of the core–shell interface. *Nano Lett.* **11**, 687–693 (2011).
116. Wang, C., Wehrenberg, B. L., Woo, C. Y. & Guyot-Sionnest, P. Light emission and amplification in charged CdSe quantum dots. *J. Phys. Chem. B* **108**, 9027–9031 (2004).
117. Haug, A. Influence of doping on threshold current of semiconductor lasers. *Electron. Lett.* **21**, 792–794 (1985).
118. Copeland, J. Heavily-doped semiconductor lasers. *IEEE J. Quantum Electron.* **17**, 2187–2190 (1981).
119. Geuchies, J. et al. Quantitative electrochemical control over optical gain in colloidal quantum-dot and quantum-well solids. *Proc. SPIE* **11464**, 114640R (2020).
120. Rinehart, J. D., Schimpf, A. M., Weaver, A. L., Cohn, A. W. & Gamelin, D. R. Photochemical electronic doping of colloidal CdSe nanocrystals. *J. Am. Chem. Soc.* **135**, 18782–18785 (2013).
121. Ivanov, S. A. et al. Light amplification using inverted core/shell nanocrystals: towards lasing in the single-exciton regime. *J. Phys. Chem. B* **108**, 10625–10630 (2004).
122. Nanda, J. et al. Light amplification in the single-exciton regime using exciton–exciton repulsion in type-II nanocrystal quantum dots. *J. Phys. Chem. C* **111**, 15382–15390 (2007).
123. Klimov, V. I. Spectral and dynamical properties of multiexcitons in semiconductor nanocrystals. *Annu. Rev. Phys. Chem.* **58**, 635–673 (2007).
124. Piryatinski, A., Ivanov, S. A., Tretiak, S. & Klimov, V. I. Effect of quantum and dielectric confinement on the exciton–exciton interaction energy in type II core/shell semiconductor nanocrystals. *Nano Lett.* **7**, 108–115 (2007).
125. Navarro-Arenas, J. et al. Single-exciton amplified spontaneous emission in thin films of $CsPbX_3$ (X=Br, I) perovskite nanocrystals. *J. Phys. Chem. Lett.* **10**, 6389–6398 (2019).
126. Ithurria, S. & Dubertret, B. Quasi 2D colloidal CdSe patelets with thicknesses controlled at the atomic level. *J. Am. Chem. Soc.* **130**, 16504–16505 (2008).
127. Talapin, D. V. et al. Seeded growth of highly luminescent CdSe/CdS nanoheterostructures with rod and tetrapod morphologies. *Nano Lett.* **7**, 2951–2959 (2007).
128. Carbone, L. et al. Synthesis and micrometer-scale assembly of colloidal CdSe/CdS nanorods prepared by a seeded growth approach. *Nano Lett.* **7**, 2942–2950 (2007).
129. Xing, G. et al. Ultralow-threshold two-photon pumped amplified spontaneous emission and lasing from seeded CdSe/CdS nanorod heterostructures. *ACS Nano* **6**, 10835–10844 (2012).
130. Di Stasio, F. et al. Single-mode lasing from colloidal water-soluble CdSe/CdS quantum dot-in-rods. *Small* **11**, 1328–1334 (2015).
131. Manfredi, G. et al. Lasing from dot-in-rod nanocrystals in planar polymer microcavities. *RSC Adv.* **8**, 13026–13033 (2018).
132. Zavelani-Rossi, M., Lupo, M. G., Krahne, R., Manna, L. & Lanzani, G. J. N. Lasing in self-assembled microcavities of CdSe/CdS core/shell colloidal quantum rods. *Nanoscale* **2**, 931–935 (2010).
133. Liao, Y., Xing, G., Mishra, N., Sum, T. C. & Chan, Y. Low threshold, amplified spontaneous emission from core-seeded semiconductor nanotetrapods incorporated into a sol–gel matrix. *Adv. Mater.* **24**, OP159–OP164 (2012).
134. Shaviv, E., Salant, A. & Banin, U. Size dependence of molar absorption coefficients of CdSe semiconductor quantum rods. *Chem. Phys. Chem.* **10**, 1028–1031 (2009).
135. Yeltik, A. et al. Experimental determination of the absorption cross-section and molar extinction coefficient of colloidal CdSe nanoplatelets. *J. Phys. Chem. C* **119**, 26768–26775 (2015).
136. Achtstein, A. W. et al. Linear absorption in CdSe nanoplates: thickness and lateral size dependency of the intrinsic absorption. *J. Phys. Chem. C* **119**, 20156–20161 (2015).
137. Karel Čapek, R. et al. Optical properties of zincblende cadmium selenide quantum dots. *J. Phys. Chem. C* **114**, 6371–6376 (2010).
138. Ithurria, S., Bousquet, G. & Dubertret, B. Continuous transition from 3D to 1D confinement observed during the formation of CdSe nanoplatelets. *J. Am. Chem. Soc.* **133**, 3070–3077 (2011).
139. Tessier, M. D., Javaux, C., Maksimovic, I., Loriette, V. & Dubertret, B. Spectroscopy of single CdSe nanoplatelets. *ACS Nano* **6**, 6751–6758 (2012).
140. Pietryga, J. M., Zhuravlev, K. K., Whitehead, M., Klimov, V. I. & Schaller, R. D. Evidence for barrierless Auger recombination in PbSe nanocrystals: a pressure-dependent study of transient optical absorption. *Phys. Rev. Lett.* **101**, 217401 (2008).
141. Htoon, H., Hollingsworth, J. A., Dickerson, R. & Klimov, V. I. Effect of zero- to one-dimensional transformation on multiparticle Auger recombination in semiconductor quantum rods. *Phys. Rev. Lett.* **91**, 227401 (2003).
142. Rabouw, F. T. et al. Reduced Auger recombination in single CdSe/CdS nanorods by one-dimensional electron delocalization. *Nano Lett.* **13**, 4884–4892 (2013).
143. Zavelani-Rossi, M., Lupo, M. G., Tassone, F., Manna, L. & Lanzani, G. Suppression of biexciton Auger recombination in CdSe/CdS dot/rods: role of the electronic structure in the carrier dynamics. *Nano Lett.* **10**, 3142–3150 (2010).
144. Gao, Y. et al. Low-threshold lasing from colloidal CdSe/CdSeTe core/alloyed-crown type-II heteronanoplatelets. *Nanoscale* **10**, 9466–9475 (2018).
145. Kelestemur, Y., Cihan, A. F., Guzelturk, B. & Demir, H. V. Type-tunable amplified spontaneous emission from core-seeded CdSe/CdS nanorods controlled by exciton–exciton interaction. *Nanoscale* **6**, 8509–8514 (2014).
146. Li, Q. & Lian, T. A model for optical gain in colloidal nanoplatelets. *Chem. Sci.* **9**, 728–734 (2018).
147. Geiregat, P. et al. Thermodynamic equilibrium between excitons and excitonic molecules dictates optical gain in colloidal CdSe quantum wells. *J. Phys. Chem. Lett.* **10**, 3637–3644 (2019).
148. Olutas, M. et al. Lateral size-dependent spontaneous and stimulated emission properties in colloidal CdSe nanoplatelets. *ACS Nano* **9**, 5041–5050 (2015).
149. Tomar, R. et al. Charge carrier cooling bottleneck opens up nonexcitonic gain mechanisms in colloidal CdSe quantum wells. *J. Phys. Chem. C* **123**, 9640–9650 (2019).
150. Homburg, O. et al. Biexcitonic gain characteristics in ZnSe-based lasers with binary wells. *Phys. Rev. B* **60**, 5743–5750 (1999).
151. Logue, F. et al. Optical gain in (Zn, Cd)Se–Zn(S, Se) quantum wells. *J. Opt. Soc. Am. B* **15**, 1295–1304 (1998).
152. Ding, J. et al. Excitonic gain and laser emission in ZnSe-based quantum wells. *Phys. Rev. Lett.* **69**, 1707–1710 (1992).
153. Diroll, B. T., Kirschner, M. S., Guo, P. & Schaller, R. D. Optical and physical probing of thermal processes in semiconductor and plasmonic nanocrystals. *Annu. Rev. Phys. Chem.* **70**, 353–377 (2019).
154. Achermann, M., Bartko, A. P., Hollingsworth, J. A. & Klimov, V. I. The effect of Auger heating on intraband carrier relaxation in semiconductor quantum rods. *Nat. Phys.* **2**, 557–561 (2006).
155. Schmitt-Rink, S., Chemla, D. S. & Miller, D. A. B. Theory of transient excitonic optical nonlinearities in semiconductor quantum-well structures. *Phys. Rev. B* **32**, 6601–6609 (1985).
156. Guzelturk, B., Pelton, M., Olutas, M. & Demir, H. V. Giant modal gain coefficients in colloidal II–VI nanoplatelets. *Nano Lett.* **19**, 277–282 (2019).
157. Sichert, J. A. et al. Quantum size effect in organometal halide perovskite nanoplatelets. *Nano Lett.* **15**, 6521–6527 (2015).
158. Ishihara, T., Takahashi, J. & Goto, T. Exciton state in two-dimensional perovskite semiconductor $(C_{10}H_{21}NH_3)_2PbI_4$. *Solid State Commun.* **69**, 933–936 (1989).
159. Aneesh, J. et al. Ultrafast exciton dynamics in colloidal $CsPbBr_3$ perovskite nanocrystals: biexciton effect and Auger recombination. *J. Phys. Chem. C* **121**, 4734–4739 (2017).
160. Ahumada-Lazo, R. et al. Emission properties and ultrafast carrier dynamics of $CsPbCl_3$ perovskite nanocrystals. *J. Phys. Chem. C* **123**, 2651–2657 (2019).
161. Eperon, G. E., Jedlicka, E. & Ginger, D. S. Biexciton Auger recombination differs in hybrid and inorganic halide perovskite quantum dots. *J. Phys. Chem. Lett.* **9**, 104–109 (2018).
162. Zhao, W. et al. Optical gain from biexcitons in $CsPbBr_3$ nanocrystals revealed by two-dimensional electronic spectroscopy. *J. Phys. Chem. Lett.* **10**, 1251–1258 (2019).
163. Wang, Y. et al. All-inorganic colloidal perovskite quantum dots: a new class of lasing materials with favorable characteristics. *Adv. Mater.* **27**, 7101–7108 (2015).
164. Huang, C.-Y. et al. $CsPbBr_3$ perovskite quantum dot vertical cavity lasers with low threshold and high stability. *ACS Photonics* **4**, 2281–2289 (2017).
165. Tessler, N., Denton, G. J. & Friend, R. H. Lasing from conjugated-polymer microcavities. *Nature* **382**, 695–697 (1996).
166. Kallinger, C. et al. A flexible conjugated polymer laser. *Adv. Mater.* **10**, 920–923 (1998).
167. Zhai, T., Zhang, X. & Pang, Z. Polymer laser based on active waveguide grating structures. *Opt. Express* **19**, 6487–6492 (2011).
168. Huang, C., Zhang, X., Wang, J. & Hong, C. Toward electrically pumped polymer lasing: light-emitting diodes based on microcavity arrays of distributed Bragg gratings. *Adv. Opt. Mater.* **6**, 1800806 (2018).
169. Kozlov, V. G., Bulović, V., Burrows, P. E. & Forrest, S. R. Laser action in organic semiconductor waveguide and double-heterostructure devices. *Nature* **389**, 362–364 (1997).
170. Akselrod, G. M. et al. Reduced lasing threshold from organic dye microcavities. *Phys. Rev. B* **90**, 035209 (2014).
171. Sandanayaka, A. S. D. et al. Toward continuous-wave operation of organic semiconductor lasers. *Sci. Adv.* **3**, e1602570 (2017).
172. Wu, J.-J., Wang, X.-D. & Liao, L.-S. Near-infrared solid-state lasers based on small organic molecules. *ACS Photonics* **6**, 2590–2599 (2019).
173. Sandanayaka, A. S. D. et al. Indication of current-injection lasing from an organic semiconductor. *Appl. Phys. Express* **12**, 061010 (2019).
174. Sharping, J. E., Kumar, P., Arnold, M. S., Hersam, M. C. & Stupp, S. I. Stimulated emission in single-walled carbon nanotubes. *Front. Opt.* https://doi.org/10.1364/FIO.2003.MT10 (2003).
175. Gaufrès, E. et al. Optical gain in carbon nanotubes. *Appl. Phys. Lett.* **96**, 231105 (2010).
176. Graf, A. et al. Electrical pumping and tuning of exciton-polaritons in carbon nanotube microcavities. *Nat. Mater.* **16**, 911–917 (2017).
177. Jia, Y. et al. Diode-pumped organo-lead halide perovskite lasing in a metal-clad distributed feedback resonator. *Nano Lett.* **16**, 4624–4629 (2016).
178. Jia, Y., Kerner, R. A., Grede, A. J., Rand, B. P. & Giebink, N. C. Continuous-wave lasing in an organic–inorganic lead halide perovskite semiconductor. *Nat. Photonics* **11**, 784–788 (2017).
179. Booker, E. P. et al. Vertical cavity biexciton lasing in 2D dodecylammonium lead iodide perovskites. *Adv. Opt. Mater.* **6**, 1800616 (2018).
180. Wang, Y.-C. et al. Flexible organometal–halide perovskite lasers for speckle reduction in imaging projection. *ACS Nano* **13**, 5421–5429 (2019).
181. Zhao, J. et al. Efficient CdSe/CdS quantum dot light-emitting diodes using a thermally polymerized hole transport layer. *Nano Lett.* **6**, 463–467 (2006).
182. Bae, W. K. et al. Multicolored light-emitting diodes based on all-quantum-dot multilayer films using layer-by-layer assembly method. *Nano Lett.* **10**, 2368–2373 (2010).
183. Schäfer, F., Reithmaier, J. P. & Forchel, A. High-performance GaInAs/GaAs quantum-dot lasers based on a single active layer. *Appl. Phys. Lett.* **74**, 2915–2917 (1999).
184. Chung, T., Walter, G. & Holonyak, N. Coupled strained-layer InGaAs quantum-well improvement of an InAs quantum dot AlGaAs–GaAs–InGaAs–InAs heterostructure laser. *Appl. Phys. Lett.* **79**, 4500–4502 (2001).
185. Huang, Z., Zimmer, M., Hepp, S., Jetter, M. & Michler, P. Optical gain and lasing properties of InP/AlGaInP quantum-dot laser diode emitting at 660 nm. *IEEE J. Quantum Electron.* **55**, 2000307 (2019).
186. Ledentsov, N. N. et al. Direct formation of vertically coupled quantum dots in Stranski-Krastanow growth. *Phys. Rev. B* **54**, 8743–8750 (1996).
187. Sun, Y. et al. Investigation on thermally induced efficiency roll-off: toward efficient and ultrabright quantum-dot light-emitting diodes. *ACS Nano* **13**, 11433–11442 (2019).

188. Moon, H., Lee, C., Lee, W., Kim, J. & Chae, H. Stability of quantum dots, quantum dot films, and quantum dot light-emitting diodes for display applications. *Adv. Mater.* **31**, 1804294 (2019).
189. Yoshida, K. et al. Joule heat-induced breakdown of organic thin-film devices under pulse operation. *J. Appl. Phys.* **121**, 195503 (2017).
190. Harvey, S. M. et al. Auger heating and thermal dissipation in zero-dimensional CdSe nanocrystals examined using femtosecond stimulated Raman spectroscopy. *J. Phys. Chem. Lett.* **9**, 4481–4487 (2018).
191. Kwak, J. et al. Bright and efficient full-color colloidal quantum dot light-emitting diodes using an inverted device structure. *Nano Lett.* **12**, 2362–2366 (2012).
192. Lim, J. et al. Influence of shell thickness on the performance of light-emitting devices based on CdSe/$Zn_{1-x}Cd_xS$ core/shell heterostructured quantum dots. *Adv. Mater.* **26**, 8034–8040 (2014).
193. Li, X. et al. Bright colloidal quantum dot light-emitting diodes enabled by efficient chlorination. *Nat. Photonics* **12**, 159–164 (2018).
194. Lim, J., Park, Y.-S., Wu, K., Yun, H. J. & Klimov, V. I. Droop-free colloidal quantum dot light-emitting diodes. *Nano Lett.* **18**, 6645–6653 (2018).
195. Mashford, B. S. et al. High-efficiency quantum-dot light-emitting devices with enhanced charge injection. *Nat. Photonics* **7**, 407–412 (2013).
196. Fu, Y., Jiang, W., Kim, D., Lee, W. & Chae, H. Highly efficient and fully solution-processed inverted light-emitting diodes with charge control interlayers. *ACS Appl. Mater. Interfaces* **10**, 17295–17300 (2018).
197. Cao, F. et al. High-efficiency, solution-processed white quantum dot light-emitting diodes with serially tacked red/green/blue units. *Adv. Opt. Mater.* **6**, 1800652 (2018).
198. Yang, Z. et al. All-solution processed inverted green quantum dot light-emitting diodes with concurrent high efficiency and long lifetime. *Mater. Horiz.* **6**, 2009–2015 (2019).
199. Bae, W. K. et al. Controlling the influence of Auger recombination on the performance of quantum-dot light-emitting diodes. *Nat. Commun.* **4**, 3661 (2013).
200. Pelton, M., Ithurria, S., Schaller, R. D., Dolzhnikov, D. S. & Talapin, D. V. Carrier cooling in colloidal quantum wells. *Nano Lett.* **12**, 6158–6163 (2012).
201. Shahnawaz et al. Hole-transporting materials for organic light-emitting diodes: an overview. *J. Mater. Chem. C* **7**, 7144–7158 (2019).
202. Dai, X. et al. Solution-processed, high-performance light-emitting diodes based on quantum dots. *Nature* **515**, 96–99 (2014).
203. Yun, J. et al. Controlling charge balance using non-conjugated polymer interlayer in quantum dot light-emitting diodes. *Org. Electron.* **50**, 82–86 (2017).
204. Pan, J. et al. Boosting the efficiency of inverted quantum dot light-emitting diodes by balancing charge densities and suppressing exciton quenching through band alignment. *Nanoscale* **10**, 592–602 (2018).
205. Shen, H. et al. Visible quantum dot light-emitting diodes with simultaneous high brightness and efficiency. *Nat. Photonics* **13**, 192–197 (2019).
206. Yoshida, K., Nakanotani, H. & Adachi, C. Effect of Joule heating on transient current and electroluminescence in pin organic light-emitting diodes under pulsed voltage operation. *Org. Electron.* **31**, 287–294 (2016).
207. Hayashi, K. et al. Suppression of roll-off characteristics of organic light-emitting diodes by narrowing current injection/transport area to 50 nm. *Appl. Phys. Lett.* **106**, 093301 (2015).
208. Sawabe, K. et al. High current densities in a highly photoluminescent organic single-crystal light-emitting transistor. *Appl. Phys. Lett.* **97**, 043307 (2010).
209. Yamamoto, H., Kasajima, H., Yokoyama, W., Sasabe, H. & Adachi, C. Extremely-high-density carrier injection and transport over 12000 A/cm² into organic thin films. *Appl. Phys. Lett.* **86**, 083502 (2005).
210. Boroumand, F. A., Hammiche, A., Hill, G. & Lidzey, D. G. Characterizing joule heating in polymer light-emitting diodes using a scanning thermal microscope. *Adv. Mater.* **16**, 252–256 (2004).
211. Montanarella, F. et al. Lasing supraparticles self-assembled from nanocrystals. *ACS Nano* **12**, 12788–12794 (2018).
212. le Feber, B., Prins, F., De Leo, E., Rabouw, F. T. & Norris, D. J. Colloidal-quantum-dot ring lasers with active color control. *Nano Lett.* **18**, 1028–1034 (2018).
213. Wallikewitz, B. H., de la Rosa, M., Kremer, J. H. W. M., Hertel, D. & Meerholz, K. A lasing organic light-emitting diode. *Adv. Mater.* **22**, 531–534 (2010).
214. Kim, H. et al. Optically pumped lasing from hybrid perovskite light-emitting diodes. *Adv. Opt. Mater.* **8**, 1901297 (2020).
215. Gwinner, M. C. et al. Integration of a rib waveguide distributed feedback structure into a light-emitting polymer field-effect transistor. *Adv. Funct. Mater.* **19**, 1360–1370 (2009).
216. Qin, W., Liu, H. & Guyot-Sionnest, P. Small bright charged colloidal quantum dots. *ACS Nano* **8**, 283–291 (2013).
217. Murray, C. B. et al. Colloidal synthesis of nanocrystals and nanocrystal superlattices. *IBM J. Res. Dev.* **45**, 47–56 (2001).
218. Carey, G. H. et al. Colloidal quantum dot solar cells. *Chem. Rev.* **115**, 12732–12763 (2015).
219. Schaller, R. D. & Klimov, V. I. High efficiency carrier multiplication in PbSe nanocrystals: Implications for solar energy conversion. *Phys. Rev. Lett.* **92**, 186601 (2004).
220. Yu, W. W., Falkner, J. C., Shih, B. S. & Colvin, V. L. Preparation and characterization of monodisperse PbSe semiconductor nanocrystals in a noncoordinating solvent. *Chem. Mater.* **16**, 3318–3322 (2004).
221. Pietryga, J. M. et al. Utilizing the lability of lead selenide to produce heterostructured nanocrystals with bright, stable infrared emission. *J. Am. Chem. Soc.* **130**, 4879–4885 (2008).
222. Du, H. et al. Optical properties of colloidal PbSe nanocrystals. *Nano Lett.* **2**, 1321–1324 (2002).
223. Schaller, R. D., Petruska, M. A. & Klimov, V. I. Tunable near-infrared optical gain and amplified spontaneous emission using PbSe nanocrystals. *J. Phys. Chem. B* **107**, 13765–13768 (2003).
224. Christodoulou, S. et al. Single-exciton gain and stimulated emission across the infrared telecom band from robust heavily doped PbS colloidal quantum dots. *Nano Lett.* **20**, 5909–5915 (2020).

Acknowledgements

Y.-S.P., J.R. and V.I.K. were supported by the Laboratory Directed Research and Development (LDRD) program at Los Alamos National Laboratory under project 20200213DR. J.R. was supported by the National Research Foundation of Korea (NRF), the Korea government (MSIT), grant No. 2020R1C1C1013079. B.T.D. and R.D.S. were supported by the U.S. Department of Energy, Office of Science, under contract no. DE-AC02-06CH11357. This work was performed, in part, at the Center for Nanoscale Materials, a U.S. Department of Energy Office of Science User Facility.

Author contributions

V.I.K. conceived the idea of the Review and developed its outline. All authors contributed to the writing and editing of the Review.

Competing interests

The authors declare no competing interests.

Publisher's note

Springer Nature remains neutral with regard to jurisdictional claims in published maps and institutional affiliations.